

## Quantum model simulations of attosecond electron diffraction

Peter BAUM<sup>1</sup>, Jörn MANZ<sup>2\*</sup> & Axel SCHILD<sup>2</sup>

<sup>1</sup>Max-Planck-Institute of Quantum Optics, and Ludwig-Maximilians-Universität München, Am Coulombwall 1, Garching 85748, Germany;

<sup>2</sup>Freie Universität Berlin, Institut für Chemie und Biochemie, Takustr. 3, Berlin 14195, Germany

Received December 7, 2009; accepted February 10, 2010; published online May 24, 2010

Ultrafast diffraction with free attosecond electron pulses promises insight into the four-dimensional motion of charge density in atoms, molecules and condensed matter. Here we consider the quantum dynamics of the electron-electron scattering process on an attosecond time scale. By numerically solving the time-dependent two-electron Schrödinger equation, we investigate the interaction of an incoming keV-range electron wavepacket by the bound electron of an aligned H<sub>2</sub><sup>+</sup> molecule, using a one-dimensional model. Our findings reveal the ratio of elastic to inelastic contributions, the role of exchange interaction, and the influence of the molecular electron density to diffraction. Momentum transfer during the scattering process, from the incoming to the bound electron mediated by the nuclei, leaves the bound electron in a state of coherent oscillation with attosecond recurrences. Entanglement causes related state-selective oscillations in the phase shift of the scattered electron. Two scenarios of distinguishable and indistinguishable free and bound electrons yield equivalent results, irrespective of the electronic spins. This suggests to employ the scenario of distinguishable electrons, which is computationally less demanding. Our findings support the possibility of using electron diffraction for imaging the motion of charge density, but also suggest the application of free electron pulses for inducing attosecond dynamics.

**ultrafast electron diffraction, scattering theory, attosecond dynamics, entanglement, coherence**

**PACS:** 03.65.Nk, 03.65.Ud, 03.65.Vf, 34.80.Kw

### 1 Introduction

Changes in matter involve the ultrafast motion of nuclei and electrons from initial to final positions within the structures of interest. The significance of reaction pathways on complex energy landscapes is, for example, evident for chemical reactions [1] and for some phase transformations [2]; whether a similar picture is appropriate for electronic transitions is currently under investigation [3–6]; see also the special issue on attosecond molecular dynamics [7] with various contributions, including refs. [8–21]. The essential time ranges on the atomic scale are femtoseconds/picoseconds for the motion of nuclei and down to attoseconds for rearrangements of charge density. The experimental investigation of such processes requires sufficient temporal resolution, but also the ability to identify the directions of motion in the three spatial dimensions.

Potent approaches for this purpose are ultrafast electron diffraction and microscopy [22], methodologies that simulta-

neously provide resolutions of femtoseconds and picometers (sub-Å). This is achieved by making use of the short matter wavelength of electrons (for example 0.07 Å at 30 keV energy), which is smaller than atomic distances. Probing a sample with ultrashort electron pulses during a change can therefore provide structural snapshots and direct visualization of the atomic-scale action (4D-imaging). Ultrafast diffraction was applied to phase transformations [2,23], laser ablation [24], nano-sized wires and particles [25,26] molecular surface layers [27], biomolecules [28], melting processes [29,30], ferroelectric materials [31], aligned molecules [32], and many other systems. This rich magnitude of findings in very different types of samples shows the importance of atomic-scale movements for understanding matter transformations. Ultrafast electron microscopy is ideal for the study of more complex specimens [33,34], for example by direct imaging [35], selected-area diffraction [36], or element-specific spectroscopy [37]; all with femtosecond timing and atomic-scale resolutions.

However, the regime of electron dynamics has so far eluded a direct visualization in four dimensions. Recently,

\*Corresponding author (email: jmanz@chemie.fu-berlin.de)

Baum and Zewail proposed how to advance ultrafast electron diffraction into the domain of electronic motion [8]. Because electrons have much less mass than nuclei, the rearrangements may take place as fast as within attoseconds; for example, an instantaneous removal of one electron from an atom or a molecule is predicted to result in rearrangements of the remaining electron density within  $\sim 50$  attoseconds [38]. Observation of such or related processes requires probe pulses of similar or shorter duration and in free space. One approach for the generation of attosecond electron pulses is based on compression in optical fields [39]. Two counter-propagating laser pulses form an intensity grating of which the individual electrons in a co-propagating electron pulse are repelled and pushed towards the optical minima. This acts as a temporal lens [40]; the electron pulses can reach durations of 15 attoseconds (and shorter) at central energies of 10–100 keV. In contrast to attosecond photon pulses at around 100 eV [41,42], these attosecond electron pulses have by factors of 1000 shorter wavelengths. Attosecond diffraction experiments seem possible [8].

The suggested experiments [8] should discover new possibilities for imaging of intramolecular electronic dynamics, with spatial and temporal resolutions in the domains below 0.1 Å and below 100 as, respectively. At the same time, they provide a new key to induce and probe these processes with ultrahigh resolutions. Both aspects pose challenges for corresponding quantum dynamics simulations of the collision induced processes, with the required spatio-temporal resolutions. From a methodologic point of view, this is a difficult task. Even if one allows the approximation that the nuclei are frozen on the time scale of the collision of the electron pulse with the target molecule or molecular ion, with typical collision times below 100 as, the quantum simulations of the planned experiments call for propagations of the representative electronic wavefunctions with energies in the keV domain, not only for the incoming electron but, in principle at least, also for the initially bound electrons which might acquire similar energies due to momentum transfer, electron exchange, and/or ionization. At very low kinetic energies in the domain of few eV, the incoming electron may excite selective short-lived resonances which induce sequel processes such as dissociative attachment [43]. Various quantum model simulations describing these processes are documented e.g. in refs. [44,45]. R-matrix propagations have been employed for simulations of electron-molecule scattering and re-scattering, at much smaller energies (in the domain of 1 – 100 eV), see e.g. refs. [46,47] and the general reviews [48,49]. For intermediate energies say 100 eV – 1 keV, one may employ the independent atom model (IAM), see e.g. refs. [50,51] and references therein. Quantum dynamics simulations of laser induced electron diffraction may also be considered as refs. [52–59], here the incoming electron pulse is prepared by a laser pulse which induces three sequential steps, (i) ionization, (ii) recollision and (iii) diffraction, somewhat analogous to the three-step-model for high harmonic generation [60];

see also refs. [14,15,17,61–67]. The maximum energy which can be achieved by laser induced diffraction is, however, limited to  $3.17 U_p$  where  $U_p$  is the ponderomotive energy—to our knowledge, it has not yet been demonstrated that laser induced diffraction can reach the keV domain [67,68].

The suggested experiments call for pioneering extensions of state-of-the-art methods for quantum model simulations of electron-molecule or -molecular ion scattering. Here we shall present the first model propagations of representative electron wavepacket dynamics in the keV domain. For this purpose, we employ a simple model system, i.e.  $e + H_2^+$  scattering, but in the keV domain. This system, and the corresponding bound system  $H_2$ , has served as a reference for developing quantum dynamical methods and demonstrations of fundamental effects in attosecond molecular dynamics, in several recent studies, including refs. [6,12–18,62,69–71].

The paper is organized as follows: In section 2, we derive a list of specific challenges for quantum dynamics simulations which are posed by the planned experiment [8]. Section 3 presents the details of the model, the numerical techniques, and also theoretical extensions of time-independent scattering theory [72] to time-dependent analyses of electron-molecule or electron-ion scattering in the keV energy domain. The results and discussions are in section 4, and the conclusions in section 5.

## 2 Experimental challenges for quantum dynamics simulations of electron diffraction in the keV domain

Our vision of an experiment consists of a condensed matter target, for example a molecular crystal, in which electron dynamics is excited (see below); attosecond electron pulses at keV-range energies and in free space are used to diffract from the charge density distribution inside the target at well-defined moments during the change [39]. For crystalline materials, Bragg spots are generated with an intensity that depends on the atomic and electronic structures within the unit cell [8]. Other schemes of attosecond imaging are also possible, ranging from measuring changes in radial scattering distributions of amorphous or gaseous samples to direct imaging of charge densities in a conceived attosecond electron microscope.

Electron pulses for diffraction must have a de Broglie wavelength shorter than atomic distances and provide Bragg conditions with experimentally convenient diffraction angles. Central energies of about 30 keV in crystalline diffraction or up to hundreds of keV in electron microscopy are therefore ideal. This energy range is by factors of 1000 higher than the binding energies that hold matter together. Even a single electron can therefore ionize the sample and extended illumination destroys the target under investigation. The ratio between useful scattering events (elastic) to radiation damage (inelastic) is, depending on definition, in the order of  $10^2 – 10^3$  in electron diffraction and microscopy [73], which is good enough to obtain clear diffraction patterns or images

from most practical samples. Whether this important ratio persists for attosecond pulses and how it compares to conventional illumination is one of the topics of this investigation.

Conclusion from diffraction patterns to electronic structures requires a clear influence of the target's electron density to the phase of the scattered electron. Usually, electron diffraction is considered as mostly resulting from the total potential of the nuclei and their electron clouds, which are assumed to be static [74]; this results in tabulated structure factors for the elements (neutral atoms and ions). An incoming electron wave obtains a phase shift as a result of the temporary retardation while passing through the scattering potential. Assemblies of multiple atoms generate interferences and result in complex spatial diffraction patterns that depend on the atomic distances. For attosecond pulses, the time to pass through a molecule or unit cell is comparable to the pulse duration. This implies a rather short time for significant energy and momentum transfer, mediated by the transient Coulomb forces to the investigated electron density during the scattering process. This could influence the charge density under investigation before suitable information is extracted. We therefore need to investigate the effect of attosecond pulses and different molecular eigenstates to diffraction, and address the significance of scattering phases on attosecond time scales.

The possibility of visualizing charge dynamics in matter by electron diffraction also calls for consideration of suitable excitation mechanisms. The use of ultrashort laser pulses, strong fields, attosecond photon pulses, or X-ray pulses from free electron lasers was mentioned [8]; here we consider the possibility of using the attosecond electron packets themselves for the purpose of inducing electron dynamics. The transfer of momentum during scattering is impulsive and can therefore induce superposition of states and oscillations of charge density. This may offer a novel possibility for inducing

attosecond dynamics in matter, without requiring energy matching to absorptive resonances and without limitation by optically dark symmetries.

The model system that we selected for our studies is the molecular hydrogen ion ( $H_2^+$ ). It is chosen as a simple but illuminating system for our questions: First, the single bound electron and the incoming keV-range scattering electron can be treated with a two-electron Schrödinger equation. Second, several excited states exist in  $H_2^+$  with different shapes of the electron density; this allows us to study the influence of changing molecular electron density on the outcome of diffraction. And third, low-dimensional approximations for the Coulomb potential were reported that are useful for saving computational effort [62]; see below. Figure 1 depicts the layout of the following investigations. The  $H_2^+$  ion is set up in the electronic ground state (a) or in the first excited state (b); the wavepacket that represents the free incoming electron (left hand side) has a kinetic energy in the keV domain, a de Broglie wavelength shorter than the internuclear distance  $R$  of the target ion, and a longitudinal width slightly larger than  $R$ , corresponding to a duration of 15 attoseconds at the instant of collision. We assume that the target ion is pre-aligned along the direction of the incoming electron pulse, e.g. by using the methods of Seideman and Stapelfeldt [75,76]. The collision time is  $\tau_{\text{col}} \approx 50$  attoseconds and the nuclei can be considered as fixed on this time scale. The transmitted electron packet will acquire state-dependent phase shifts as a result of the scattering potential; the collision may also induce excitations/de-excitations, momentum transfer, and entanglement of the two electrons. All these consequences are discussed below in detail. Although our envisioned first experiments will use molecular crystals, the investigation of a single molecule is valuable, because generalization to crystalline diffraction is possible for many cases.

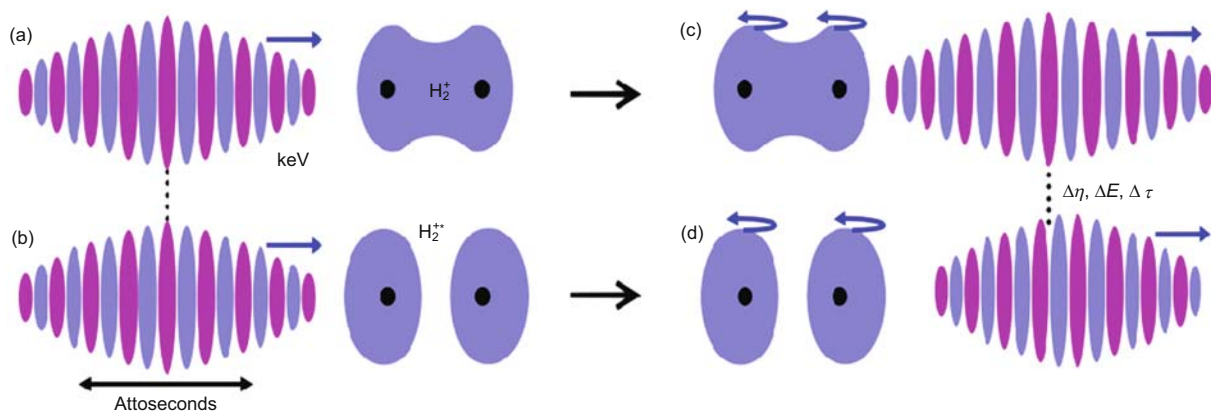


**Figure 1** Schematics of the investigated attosecond diffraction experiment. An attosecond electron packet at  $E_{\text{kin}} = 1.5$  keV, with a de Broglie wavelength of  $\lambda = 0.3$  Å, and with a duration of 15 as is scattered from  $H_2^+$  in (a) the electronic ground state and (b) an excited state. (c), (d) The collision induces momentum transfer mediated by the nuclei, causing weak, quasi-periodic electronic transitions in the target ion (indicated by two little curved arrows), whereas the electronic wavepacket of the free electron is diffracted into the forward direction with state-selective phase shifts  $\eta$ , scattering delay times  $\tau$ , and shifts of the mean kinetic energy  $\Delta E$ . In addition, the ultrafast electron-electron interaction during collision may cause coherent electronic motions in the target ion, which are entangled with quasi-periodic temporal variations of the phase shifts for the scattered electron (see the text).

In order to have our simulations reflect the experimental conditions, we require several settings that are uncommon in scattering theory. First, the scattering electron experimentally always has a constant energy irrespectively of the target state; this results in a total energy of the system that is not constant when changing the initial states of the sample. Second, the incoming attosecond wavepacket needs to be set up with an energy-time correlation (chirp), i.e. with a momentum distribution that squeezes the duration to the Fourier-limited minimum when reaching the molecule [39]; the packet width there should cover the internuclear distance of the target ion. Third, the generation of keV electrons by the photoelectric effect and subsequent acceleration happens about one meter apart from the target ion with its bound electron. This suggests to consider and compare two scenarios—the first one for distinguishable electrons, the other one for the ubiquitous indistinguishable ones. Fourth, the quantum model simulations should explain why the spin of the scattered electrons has no significant influence in many diffraction experiments at kinetic energies in the keV domain; in fact, the spin is not defined in typical experimental arrangements. In the following we shall discuss how we meet these challenges with our simulations, and discuss the results thereafter.

### 3 Theory, model and techniques

Our quantum simulations of  $e + H_2^+$  scattering employ the model which has been developed by Bandrauk and coworkers in order to describe excitations and photoionization of an  $H_2$  molecule which is aligned along the laboratory-fixed  $z$ -coordinate, by means of a linearly- $z$ -polarized laser pulse, starting from the ground state  ${}^1\Sigma_g^+$  [62]. Here we add extension for the two scenarios which are suggested by the experimental setup (section 2). Both assume that the two electrons have arbitrary spins. We shall neglect, however, any spin interactions during the ultrafast collision, i.e. we focus on the time evolution of the spatial wavefunction, disregarding any changes of the spin function.

The first scenario assumes that initially, the free electron (labelled “1”) is distinguishable from the bound electron (labelled “2”) in the target  $H_2^+$  ion, i.e. the initial spatial wavefunction can be written as Hartree product, see eq. (6) below. This ansatz is taylored to the experimental situation where both electrons are prepared independently at large distances from each other. In contrast, the second scenario assumes that both electrons are indistinguishable i.e. the nuclear spatial and spin wave functions are symmetric and anti-symmetric for a singlet state, and vice versa for a triplet state. The implicit assumption for this second scenario is that the wavefunctions of electrons are always anti-symmetric, from the outset of the universe, irrespective of the experiment. It is helpful to start with model simulations for the first scenario of distinguishable electrons, because the numerical requirements are much less than for the second one (see the discussion after eq. (29) below). In fact, the spatial wave-

function for the second scenario can be constructed later on, simply by symmetrizing or antisymmetrizing the non-symmetric wavefunction for the first scenario, see eq. (41) below. Efficient construction of a wavefunction for indistinguishable particles by means of (anti-)symmetrization of a non-symmetric wavefunctions for distinguishable particles have been demonstrated previously in ref. [77]. Later on, we shall also discuss the second scenario. It will turn out that for the experimental conditions, with total mean energy  $E_{\text{tot}}$  much larger than the ionization potential IP, both scenarios yield essentially equivalent results. This will support our preferential consideration of the first scenario of distinguishable electrons, a posteriori.

In the frame of the model of Bandrauk et al. [62], it is assumed that the nuclei of the  $H_2^+$  ion are aligned along the laboratory  $z$ -axis, and the incoming electron “1” moves along that  $z$ -axis, with coordinate  $z_1$ . Anticipating that the interaction of electron “1” with the target  $H_2^+$  is ultrafast, i.e. in the time domain below 100 as, we assume that the nuclei are frozen at their equilibrium distance  $R = 1.0520 \text{ \AA}$ . Choosing a coordinate system which has its origin at the center of mass of the two protons, they are thus located at fixed positions  $Z_1 = -R/2$  and  $Z_2 = +R/2$ . Marginal motions of the center of masses of the total system (two protons plus two electrons), due to the motions of the electrons, are neglected in the present extension of the model of Bandrauk et al. Finally, the second electron “2” which is initially embedded in the target,  $H_2^+$  in its electronic ground state, is also constrained to move along the  $z$ -axis, with coordinate  $z_2$ . Altogether, the model of Bandrauk et al. [62] is thus physically one-dimensional (1D) but mathematically 2D. Using SI units, the corresponding model Hamiltonian is thus

$$H = T + V = T_1 + T_2 + V(z_1, z_2) \quad (1)$$

with kinetic energy operators  $T_l = -\frac{\hbar^2}{2m_e} \frac{\partial^2}{\partial z_l^2}$  for electrons  $l = 1, 2$ . In order to account for physical 3D effects, the electronic interaction potential is modelled as sum of soft Coulomb (sC) potentials,

$$\begin{aligned} V_{\text{sC},H_2} &= V^{(0)} + V^{(1)} \\ &= \sum_{l=1}^2 \sum_{n=1}^2 V_{\text{sC},en}(|z_l - Z_{\text{nul}}|) + V_{\text{sC},ee}(|z_1 - z_2|) \\ &= \frac{1}{4\pi\epsilon_0} \left( \sum_{l=1}^2 \left[ -\frac{1}{\sqrt{(z_l + R/2)^2 + c}} - \frac{1}{\sqrt{(z_l - R/2)^2 + c}} \right] \right. \\ &\quad \left. + \frac{1}{\sqrt{(z_1 - z_2)^2 + d}} \right), \end{aligned} \quad (2)$$

where the first term  $V^{(0)}$  represents soft Coulomb attraction of the electrons ( $e$ )  $l$  to the nuclei ( $n$ ), whereas the last term  $V^{(1)}$  describes soft Coulomb repulsion of the electrons. For convenience, the Coulomb repulsion  $(4\pi\epsilon_0 R)^{-1}$  between the frozen nuclei is omitted in eq. (2) because in the present model, it is a constant that does not effect the results for the electron dynamics. The parameters  $c = 0.20 \text{ \AA}^2$  and  $d = 0.34654 \text{ \AA}^2$

have been adjusted so that the model reproduces the excitation energies for transitions to the first two excited singlet states [62].

The soft Coulomb potential (2) is illustrated in Figure 2. Apparently, it has two minima with values

$$V_{\text{SC},\text{H}_2,\text{min}} = V_{\text{SC},\text{H}_2}(\pm R/2, \mp R/2) = -78.34 \text{ eV} \quad (3)$$

at  $z_1 = -z_2 = \pm R/2$ , due to the attractions of two different electrons to two different nuclei, as well as steep ridges along the line  $z_1 = z_2 \rightarrow \pm \infty$ , accounting for (soft) Coulomb repulsion between the electrons in the asymptotic domains. For large distances of the electron “1” from  $\text{H}_2^+$ ,  $z_1 \rightarrow -\infty$  or  $z_1 \rightarrow +\infty$ ,  $V(z_1, z_2)$  approaches the soft Coulomb potential describing the “reactant” or “product” ion,  $\text{H}_2^+$  with electron “2”,

$$\begin{aligned} V_{\text{SC},\text{H}_2}(z_1, z_2) &\rightarrow V_{\text{SC},\text{H}_2^+}(z_2) \\ &= \frac{1}{4\pi\epsilon_0} \left( -\frac{1}{\sqrt{(z_2 + R/2)^2 + c}} - \frac{1}{\sqrt{(z_2 - R/2)^2 + c}} \right) \\ &\quad \text{for } z_1 \rightarrow \pm\infty. \end{aligned} \quad (4)$$

It is shown in Figure 3, together with the three lowest eigenenergies  $E_l$  and the orthonormal eigenfunctions  $\phi_l(z_2)$ , which are obtained as solutions of the “asymptotic” Schrödinger equation

$$(T_2 + V_{\text{H}_2^+}(z_2))\phi_l(z_2) = E_l\phi_l(z_2). \quad (5)$$

Gratifyingly, the values for the excitation energy for transition to the first excited state  $E_1 - E_0$  as well as the ionization

potential IP =  $-E_0$ , i.e. 12.8 eV and 38.4 eV, agree reasonably well with experimental and quantum chemical reference values 11.8 eV and 41.5 eV [78], respectively. The model of Bandrauk et al. describes not only the energetics of  $\text{H}_2$  [62], but also of  $\text{H}_2^+$  rather well.

For the first scenario of distinguishable electrons, the normalized initial (“in”) spatial wavefunction

$$\Psi_{l,k,\sigma}(z_1, z_2, t_{\text{in}}) = g_{k,\sigma}(z_1)\phi_l(z_2) \quad (6)$$

at time  $t = t_{\text{in}}$  is modelled as the product of a Gaussian (“g”) wavefunction  $g_{k,\sigma}(z_1)$  describing the incoming electron “1” times the eigenfunction  $\phi_l(z_2)$  of electron “2” in the target  $\text{H}_2^+$  in electronic state  $l$ , respectively. The Gaussian for the incoming electron “1” is characterized by the mean value of the momentum

$$p = \hbar k \quad (7)$$

with corresponding de Broglie wave length

$$\lambda = \frac{2\pi}{k} \quad (8)$$

and asymptotic (“asym”, experimental) kinetic energy

$$E_{\text{kin,asym}} = \frac{p^2}{2m_e}, \quad (9)$$

and the width parameter  $\sigma$ . In accord with the experimental setup (section 2), it is designed such that it is squeezed to the minimum width (= twice the standard deviation)

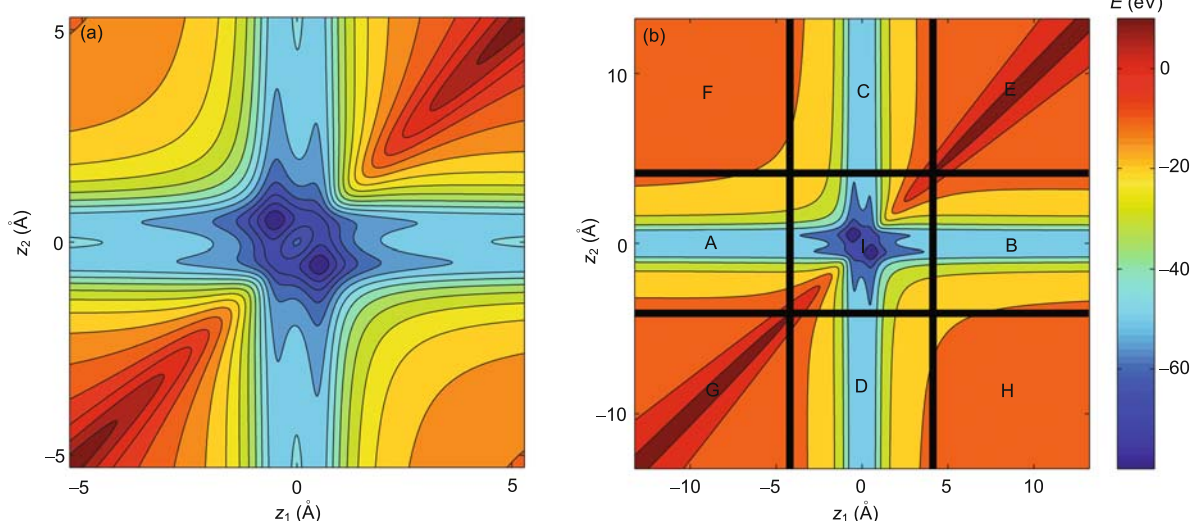


**Figure 2** (a) Soft Coulomb potential for  $\text{H}_2$  in the electronic ground state for equilibrium bond distance  $R = 1.0520 \text{ \AA}$ , eq. (2), adapted from ref. [62]. Equipotential contours are labeled by colour codes. (b) Various domains of the soft Coulomb potential, which correspond to different possible scattering events, including domains A for the incoming wavepacket and back-scattering of electron “1”, I for strong interaction (I) of all particles, B for forward-scattering of electron “1”, C for exchange of electrons and forward scattering of electron “2”, D for exchange of electrons and backward scattering of electron “2”. The other four domains E, F, G, H correspond to four cases of electron scattering and ionization, specifically for forward, backward, backward and forward scatterings of electron “1” and simultaneous ionization of electron “2” into the forward, forward, backward, and backward directions, respectively.

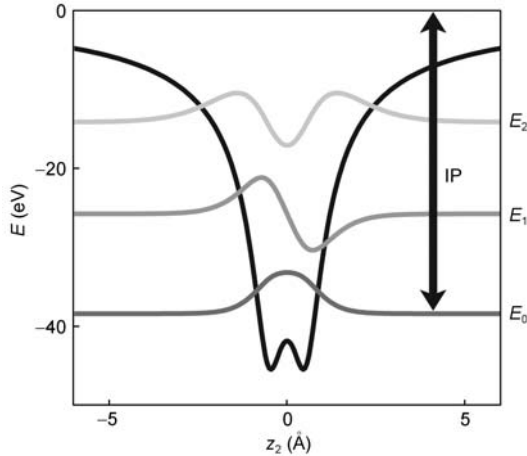


**Figure 3** Soft Coulomb potential for  $\text{H}_2^+$  in the electronic ground state, for the equilibrium bond distance of  $\text{H}_2$  as in Figure 2, eq. (4), adapted from ref. [62]. Also shown are the three lowest eigenfunctions  $\phi_l(z_2)$ , with baselines adjusted to the eigenenergies  $E_l$  of the three lowest electronic eigenstates, cf. eq. (5).

$$\delta z_0 = 2\sigma = \sqrt{\frac{1}{\alpha_0}} \quad (10)$$

at the instant of collision. That instant is defined as time  $t = 0$ , with mean value of the coordinate  $z_1$  equal to zero. Subsequently, we define  $\delta z_0$  as “target” width. For convenience, eq. (10) defines the parameter  $\alpha_0$  which will be used below. Rigorously,  $g_{k,\sigma}(z_1)$  should be modeled as wavepacket which is launched at time  $t_{\text{in}} \rightarrow -\infty$  in the far asymptotic domain  $z_1 \rightarrow -\infty$ , with asymptotic momentum  $p = \hbar k$ , approaching  $\text{H}_2^+$  in the soft Coulomb potential (2). Numerical constraints call for additional approximations (see below), i.e. we have to start our simulations at finite time  $t_{\text{in}} < 0$ . In practice, we employ the normalized initial wavefunction [79]

$$g_{k,\sigma}(z_1) = N_{t_{\text{in}}} \exp\left(-\alpha_{t_{\text{in}}}(z - z_{\text{in}})^2 + ik_{t_{\text{in}}}(z - z_{\text{in}}) + \frac{i}{\hbar}\gamma_{t_{\text{in}}}\right) \quad (11)$$

with parameters

$$N_{t_{\text{in}}} = (2 \operatorname{Re} \alpha_{t_{\text{in}}} \pi)^{1/4} \quad (12)$$

for the normalization,

$$\alpha_{t_{\text{in}}} = \frac{\alpha_0}{1 + (2i\hbar\alpha_0 t_{\text{in}}/m_e)} \quad (13)$$

for the width parameter, implying the initial width

$$\delta z_{\text{in}} = \sqrt{\frac{1 + 4\hbar^2\alpha_0^2 t_{\text{in}}^2/m_e^2}{\alpha_0}}, \quad (14)$$

$$\hbar k_{t_{\text{in}}} = \sqrt{2m_e E_{\text{kin}}} \quad (15)$$

for the mean value of the momentum,

$$z_{\text{in}} = \frac{\hbar k_{t_{\text{in}}}}{m_e} t_{\text{in}} \quad (16)$$

for the initial center of the Gaussian wavepacket, and

$$\gamma_{t_{\text{in}}} = \frac{(\hbar k)^2}{2m_e} t_{\text{in}} + \frac{i\hbar}{2} \ln\left(1 + \frac{2i\hbar\alpha_0 t_{\text{in}}}{m_e}\right) \quad (17)$$

for the phase. The initial time  $t_{\text{in}}$  is chosen such that the initial center  $z_{\text{in}}$  of the wavefunction is in the near asymptotic domain. Here, the interaction energy between the incoming electron and the  $\text{H}_2^+$  projectile may be approximated as soft Coulomb interaction between the charge of the incoming electron and the net charge of the  $\text{H}_2^+$  ion. This loss of potential energy equals the gain of kinetic energy of electron “1”, on its way from  $z_1 \rightarrow -\infty$  to  $z_{\text{in}}$ . The initial kinetic energy of the system is, therefore, approximated by

$$E_{\text{kin}} \approx E_{\text{kin,asym}} - V^{(1)}(|z_{\text{in}}|). \quad (18)$$

The result (18) determines the initial momentum, cf. eq. (15). Accordingly, the maximum kinetic energy which one of the two electrons can ever achieve, in the soft Coulomb potential is

$$E_{\text{kin,max}} = E_{\text{kin,asym}} - V_{\text{S,C,H}_2,\text{min}}. \quad (19)$$

The corresponding maximum and minimum values of the momentum and the de Broglie wavelength are

$$p_{\text{max}} = \hbar k_{\text{max}} = \sqrt{2m_e E_{\text{kin,max}}} \quad (20)$$

and

$$\lambda_{\text{min}} = \frac{2\pi}{k_{\text{max}}}, \quad (21)$$

respectively. Likewise, the maximum total energy which the wavefunction could ever encounter is for the (hypothetical) situation where the two electrons hit each other with maximum kinetic energy and with maximum soft Coulomb repulsion,

$$E_{\text{max}} = E_{\text{kin,max}} + \frac{e^2}{4\pi\epsilon_0 d}. \quad (22)$$

The ansatz (11) for the initial wavefunction describing the incoming electron “1” has been adapted from the expression for a free particle that would evolve from  $z_1 = z_{\text{in}}$  at time  $t_{\text{in}}$  to  $z_1 = 0$  at  $t = 0$ , with corresponding change of the width parameter from  $\alpha_{t_{\text{in}}}$  to  $\alpha_0$  [79]. We have tested the validity of this approximation by comparisons of the propagations of the wavefunctions for the free particle and for the particle which evolves in the soft Coulomb potential. Any deviations are, indeed, just marginal. In particular, both wavefunctions arrive at  $z_1 = 0$  very close to  $t = 0$ , with maximum albeit modest squeezing of the initial width (14) to  $2\sigma$  or close to  $2\sigma$ , eq. (10).

The time evolution of the wavefunction in the soft Coulomb potential (2), starting from the “initial” wavefunction (6)–(18), is evaluated by propagating the time dependent Schrödinger equation

$$i\hbar \frac{d}{dt} \Psi_{l,k,\sigma}(z_1, z_2, t) = H \Psi_{l,k,\sigma}(z_1, z_2, t) \quad (23)$$

from  $t = t_{\text{in}}$  via the instant of the collision ( $t = 0$ ) till the time after the collision, i.e. when most part of the wavefunction has left the domain I of strong interactions, cf. Figure 2(b). The choice of the initial state (6) is indicated by the subscripts for the quantum numbers and parameters  $l, k, \sigma$ . The effects of the kinetic and potential energy operators  $T$  and  $V$  of  $H$ , eq. (1), are evaluated in momentum and coordinate representations of the wavefunction, respectively, mediated by fast Fourier transformation (FFT) and inverse FFT, respectively [80–83], using the program package WAVEPACKET written by Schmidt and Lorenz [84]. For this purpose, the wavefunction is represented, first of all, on a large square grid with  $N_{\text{grid}} \times N_{\text{grid}}$  equally spaced grid points in the domain  $z_{1,\min} < z_1 < z_{1,\max}; z_{2,\min} < z_2 < z_{2,\max}$ , with  $z_{1,\max} - z_{1,\min} = z_{2,\max} - z_{2,\min}$ . For analysis of all the possible processes of  $e + H_2^+$  scattering with corresponding wavepackets that might penetrate into the various domains A–H shown in Figure 2(b), we set  $z_{2,\max} = -z_{2,\min}$  but  $z_{1,\max} > -z_{1,\min}$ . A possible diminution to a smaller grid is discussed below, see the paragraph after eq. (29). Adequate numerical representations of the wavefunction call for sufficiently fine grids, with spacings

$$\Delta z < \frac{\lambda_{\min}}{2} \quad (24)$$

i.e. with at least two grid points per minimum wavelengths. A small inverted-L-shaped domain close to the edges, from  $z_{\max} - z_{\text{gobbler}}$  till  $z_{\max}$ , is considered as “gobbler” domain, or domain of absorbing boundary that may cause numerical artifacts such as backscattering. In order to avoid these artifacts, the subsequent results are for times when the wavefunction  $\Psi(z_1, z_2, t)$  has not yet penetrated into the domain of the absorbing boundaries — it is, therefore, not necessary to specify any numerical implementations of “gobblers” or “absorbing boundaries”, see e.g. refs. [80,85], respectively. In practice, this condition is verified by calculating the norm of the wavefunction on the grid without the domain for the absorbing boundary, with the condition that the value for the norm should be close to 1, within a limit of  $\epsilon_{\text{norm}} = 10^{-6}$ . For the time propagation, we employ the ubiquitous split-operator method [81], with time increment  $\Delta t$  that should satisfy the Nyquist criterion [86]

$$\Delta t \leq \frac{\hbar}{E_{\max}}, \quad (25)$$

where  $E_{\max}$  is the maximum energy (22).

From the wavefunction  $\Psi_{l,k,\sigma}(z_1, z_2, t)$ , we calculate the density

$$\rho_{l,k,\sigma}(z_1, z_2, t) = |\Psi_{l,k,\sigma}(z_1, z_2, t)|^2 \quad (26)$$

as well as the flux density

$$j_{l,k,\sigma}(z_1, z_2, t) = \begin{pmatrix} j_{1,l,k,\sigma}(z_1, z_2, t) \\ j_{2,l,k,\sigma}(z_1, z_2, t) \end{pmatrix} \quad (27)$$

with components

$$j_{n,l,k,\sigma}(z_1, z_2, t) = -i \frac{\hbar}{2m_e} \left( \Psi_{l,k,\sigma}(z_1, z_2, t)^* \frac{\partial}{\partial z_n} \Psi_{l,k,\sigma}(z_1, z_2, t) - \Psi_{l,k,\sigma}(z_1, z_2, t) \frac{\partial}{\partial z_n} \Psi_{l,k,\sigma}(z_1, z_2, t)^* \right). \quad (28)$$

Moreover, integrating the densities in the various domains  $X = A, B, C, \dots$  of the soft Coulomb potential Figure 2(b) yields the corresponding probabilities or populations

$$P_{X,l,k,\sigma}(t) = \int_X dz_1 dz_2 \rho_{l,k,\sigma}(z_1, z_2, t). \quad (29)$$

It turns out that all probabilities for scattering processes involving ionization and/or electron exchange are negligible, cf. section 4, i.e. all populations of the domains C, D, E – H are close to zero. For the remaining domains  $X = A, I, B$ , for the incoming electron, strong interaction and forward scattering it suffices to propagate the wavefunction on a rather narrow rectangular ( $r$ ) grid that covers these domains and which is symmetric with respect to the  $z_1$ -axis,  $z_{r,1,\min} = z_{1,\min} \leq z_1 \leq z_{r,1,\max}$ , with  $z_{r,1,\max} \geq z_{1,\max}$  and  $z_{r,2,\min} \leq z_2 \leq z_{r,2,\max}$  with  $-z_{r,2,\min} = z_{r,2,\max} \ll z_{2,\max}$ . For the case where  $z_{r,1,\max} = z_{1,\max}$ , the diminution of the large square grid to the small rectangular one implies an enormous reduction of computer time and storage requirements, by an approximate factor of  $z_{2,\max}/z_{r,2,\max}$ . Note that this reduction is possible only for the first scenario of distinguishable electrons “1” and “2”, but not for the second one, because indistinguishable electrons penetrate not only into domains A and B for forward and backward scattering of electron “1”, but due to the symmetrization or antisymmetrization of the spatial wavefunction for electrons “1” and “2”, they enter also the domains C and D for forward and backward scattering of the “exchanged” electron “2”. The subsequent discussion continues for the first scenario, but with the wavefunction restricted to domains A, I, B.

In the asymptotic domain  $z_1 \rightarrow \infty$ , the wave function may be expanded in terms of the eigenfunctions  $\phi_n(z_2)$  of the product  $H_2^+$

$$\Psi_{l,k,\sigma}(z_1, z_2, t) \rightarrow \sum_n \Theta_{n,l,k,\sigma}(z_1, t) \phi_n(z_2) \quad (30)$$

with translational ( $\Theta$ ) wavefunctions

$$\Theta_{n,l,k,\sigma}(z_1, t) = \int dz_2 \phi_n(z_2) \Psi_{l,k,\sigma}(z_1, z_2, t). \quad (31)$$

Integrating the corresponding translational densities yields the  $n \leftarrow l$  transition probabilities i.e. the populations of the product states  $\phi_n(z_2)$  depending on the initial state (6),

$$P_{n,l,k,\sigma}(t) = \int dz_1 |\Theta_{n,l,k,\sigma}(z_1, t)|^2. \quad (32)$$

Asymptotically for  $t \rightarrow \infty$ , the  $P_{n,l,k,\sigma}(t)$  approach constant values  $P_{n,l,k,\sigma}$ . In practice, convergence

$$P_{n,l,k,\sigma}(t) \rightarrow P_{n,l,k,\sigma} \quad (33)$$

is achieved as soon as the wavefunction  $\Psi_{l,k,\sigma}(z_1, z_2, t)$  is in the near asymptotic domain.

The asymptotic expansion (30) which yields the time-independent  $n \leftarrow l$  transition probabilities (33) is a standard tool of analysis in time-independent scattering theory [72]. Here we suggest to extend this asymptotic analysis to a time-dependent one, allowing to monitor the build-up of the transition probabilities (33) as a consequence of electron-electron interaction during collision. For this purpose, the asymptotic expansion (30) is replaced with the ansatz

$$\begin{aligned} \Psi_{l,k,\sigma}(z_1, z_2, t) &= \sum_n c_{n,l,k,\sigma}^{(\text{unc})}(t) \Psi_{n,k,\sigma}^{(\text{unc})}(z_1, z_2, t) \\ &\quad + \sum_n c_{n,l,k,\sigma}^{(\text{cor})}(t) \Psi_{n,k,\sigma}^{(\text{cor})}(z_1, z_2, t) \end{aligned} \quad (34)$$

i.e.  $\Psi_{l,k,\sigma}(z_1, z_2, t)$  is decomposed into a sum of time-dependent orthogonal partial waves for “uncorrelated” (unc) and “correlated” (cor) electrons “1” and “2”, with time dependent coefficients, for all times. The absolute squares of these coefficients may be interpreted as  $n \leftarrow l$  transition probabilities for occupying the “uncorrelated” and “correlated” partial waves,

$$\begin{aligned} P_{n,l,k,\sigma}^{(\text{unc})}(t) &= |c_{n,l,k,\sigma}^{(\text{unc})}(t)|^2, \\ P_{n,l,k,\sigma}^{(\text{cor})}(t) &= |c_{n,l,k,\sigma}^{(\text{cor})}(t)|^2. \end{aligned} \quad (35)$$

Asymptotically, the sum of these transition probabilities (35) should approach the overall transition probabilities,

$$P_{n,l,k,\sigma}^{(\text{unc})}(t) + P_{n,l,k,\sigma}^{(\text{cor})}(t) \rightarrow P_{n,l,k,\sigma}. \quad (36)$$

The uncorrelated normalized partial waves are constructed by deleting the term which causes electron correlation in the Hamiltonian (1) — obviously this is the electron-electron interaction  $V^{(1)} = V_{\text{SC,ee}}(|z_1 - z_2|)$ . In fact, without  $V^{(1)}$ , the Hamiltonian (1) reduces to the separable Hamiltonian

$$\begin{aligned} H^{(0)} &= T_1 + T_2 + V^{(0)}(z_1, z_2) \\ &= T_1 + \sum_{\text{nul}=1}^2 V_{\text{SC,en}}(|z_1 - Z_{\text{nul}}|) + T_2 \\ &\quad + \sum_{\text{nul}=1}^2 V_{\text{SC,en}}(|z_2 - Z_{\text{nul}}|) \\ &= T_1 + V_{\text{SC,H}_2^+}(z_1) + T_2 + V_{\text{SC,H}_2^+}(z_2) \\ &= H_1^{(0)} + H_2^{(0)}, \end{aligned} \quad (37)$$

The “uncorrelated” partial waves are the solutions of the time-dependent Schrödinger equation with zero-order Hamiltonian  $H^{(0)}$ ,

$$i\hbar \frac{d}{dt} \Psi_{n,k',\sigma}^{(\text{unc})}(z_1, z_2, t) = H^{(0)} \Psi_{n,k',\sigma}^{(\text{unc})}(z_1, z_2, t) \quad (38)$$

starting from the same type of initial wavefunctions (6), with the constraint that all partial wave should have the same mean total energy, thus

$$E_n + \frac{(\hbar k')^2}{2m_e} = E_l + \frac{(\hbar k)^2}{2m_e}. \quad (39)$$

Since the energy gaps between the electronic levels of  $\text{H}_2^+$  (cf. Figure 3) are much smaller than the kinetic energies, the momenta  $\hbar k$  and  $\hbar k'$  are about equal. In practice, the  $\Psi_{l,k,\sigma}^{(\text{unc})}(z_1, z_2, t)$  are propagated using the same numerical techniques as for the evaluations of the  $\Psi_{l,k,\sigma}(z_1, z_2, t)$ , eq. (23). The time-dependent coefficients are then determined as

$$c_{n,l,k,\sigma}^{(\text{unc})}(t) = \int dz_1 dz_2 \Psi_{n,k',\sigma}^{(\text{unc})}(z_1, z_2, t)^* \Psi_{l,k,\sigma}(z_1, z_2, t). \quad (40)$$

The “correlated” partial waves are determined by subtracting the “uncorrelated” ones from the total wavefunction, and projecting the remainders on the eigenfunctions  $\phi_n(z_2)$  of electron 2 in the  $\text{H}_2^+$  ion. Renormalization yields the coefficients  $c_{n,l,k,\sigma}^{(\text{cor})}$ .

The partial waves (34), or any superpositions of these partial waves, may be used to analyze the reaction, by the same way as the total wavefunctions (6), e.g. one may calculate the corresponding densities, or the flux densities, or the probabilities in various domains, in accord with eqs. (26)–(29).

Finally, once one has calculated and analyzed the non-symmetric wavefunction  $\Psi_{l,k,\sigma}(z_1, z_2, t)$  for distinguishable electrons, the singlet or triplet spatial wavefunction for indistinguishable electrons are calculated by symmetrization (+) or antisymmetrization (-), respectively,

$$\Psi_{l,k,\sigma,\pm}(z_1, z_2, t) = \frac{1}{\sqrt{2}} [\Psi_{l,k,\sigma}(z_1, z_2, t) \pm \Psi_{l,k,\sigma}(z_2, z_1, t)]. \quad (41)$$

Before presenting the results of  $e + \text{H}_2^+$  scattering, let us summarize the numerical requirements for propagation of the wavefunction, exemplarily for an initial state with asymptotic kinetic energy  $E_{\text{kin,max}} = 1.5 \text{ keV}$ , width parameter  $\sigma = 1.588 \text{ \AA}$  and initial time  $t_{\text{in}} = -60.5$  as corresponding to  $z_{\text{in}} = -13.89 \text{ \AA}$ , in the near asymptotic domain. The minimum value of the soft Coulomb potential is  $V_{\text{SC,H}_2,\text{min}} = -78.34 \text{ eV}$  (eq. (3)). The maximum kinetic energy is, therefore,  $E_{\text{kin,max}} = 1578.34 \text{ eV}$  (eq. (19)), implying the minimum de Broglie wavelength  $\lambda_{\text{min}} = 0.309 \text{ \AA}$  (eq. (21)). This calls for spatial grid spacings  $\Delta z$  below  $0.155 \text{ \AA}$  (eq. (24)). In practice we employ the value  $\Delta z = 0.121 \text{ \AA}$ . The initial location at  $z_{\text{in}}$  and the initial width  $\delta z_{\text{in}}$  (14) requires a lower boundary of the grid,  $z_{1,\text{min}} < z_{\text{in}} - \delta z_{\text{in}} = -17.0 \text{ \AA}$ . We use  $z_{1,\text{min}} = -39.7 \text{ \AA}$ . As upper grid boundary for  $z_1$ , we employ  $z_{1,\text{max}} = 145.4 \text{ \AA}$  — this is large enough to allow the subsequent rather detailed analyses of the effects of  $e + \text{H}_2^+$  scattering in the near asymptotic domain. Accordingly, quantum dynamics simulations of

the wavefunction representing the two electrons on a square grid call for grid boundaries  $-z_{2,\min} = z_{2,\max} = 92.6 \text{ \AA}$  for the complementary motions of electron “2” along  $z_2$ . The “gobbler” domain starts at  $z_{\text{gobbler}} = 2.65 \text{ \AA}$  away from the grid boundary. As a consequence, there are  $N_{\text{grid}} = (z_{1,\max} - z_{1,\min})/\Delta z = 1536$  grid points along  $z_1$ , and the square spatial grid for propagation of the wavepacket consists of  $N_{\text{grid}}^2 = 2359296$  points.

Moreover, the maximum energy  $E_{\text{max}}$  is estimated as 1.600 keV (eq. (22)), calling for time steps  $\Delta t < 2.6$  as (eq. (25)). We use  $\Delta t = 0.24$  as. For a rough estimate of the corresponding number of time steps  $N_{\text{time}}$  which are needed for the quantum dynamics simulation of  $e + H_2^+$  scattering on the grid, we consider the time interval from the initial time  $t_{\text{in}}$  till the “upper” time limit  $t_{\text{up}}$  which would be required for a free particle in order to run along  $z_1$ , from the lower to the upper grid boundaries (without the gobbler domains), with speed  $\hbar k/m_e$ ,

$$t_{\text{up}} - t_{\text{in}} = \frac{z_{1,\max} - z_{\text{gobbler}} - z_{\text{in}}}{\hbar k/m_e} = 654 \text{ as}, \quad (42)$$

hence  $N_{\text{time}} \approx (t_{\text{up}} - t_{\text{in}})/\Delta t = 2725$ . Obviously, the rather large numbers of spatial and temporal grid points impose rather tough computational demands, which are close to the limits of our resources.

## 4 Results of the quantum model simulations and discussions

The presentation of the results for the quantum model simulations starts with the first scenario of an incoming electron “1” that is distinguishable from the other electron “2”, which rests in the electronic ground state of the  $H_2^+$  ion. The initial wavepacket has the form of eqs. (6), (11), i.e. it is modeled as Gaussian wavepacket times the eigenfunction for the free and bound electrons “1” and “2”, respectively. The parameters are chosen such that, on one hand, the initial wave function is taylored to the experimental situation as much as possible (cf. section 2), and on the other hand, its propagation copes with the numerical requirements and resources. As a compromise, let us consider first the example where the initial Gaussian wavefunction (11) representing the incoming electron is centered in the near asymptotic domain at  $z_{\text{in}} = -13.89 \text{ \AA}$ , with width parameter  $\sigma = 1.588 \text{ \AA}$  and asymptotic kinetic energy  $E_{\text{kin,asym}} = 1.5 \text{ keV}$ . Extrapolations to typical experimental values of about 30 keV (cf. section 2) will be discussed below. In any case, the choice of the exemplary parameters imply that  $V^{(1)}(|z_{\text{in}}|) = -1.036 \text{ eV}$  (eq. (2)),  $E_{\text{kin}} = 1501.0 \text{ eV}$  (eq. (18)),  $\hbar k/m_e = 0.230 \text{ \AA/as}$  (eq. (15)), and  $t_{\text{in}} = -60 \text{ as}$  (eq. (16)). The initial width is, therefore,  $\delta z_{\text{in}} = 3.206 \text{ \AA}$  (eq. (14)). As explained in section 3, the wavefunction is designed such that it arrives at the origin i.e. in the center of the interaction domain “I” at time  $t = 0$ . At the same time, the widths is squeezed from its initial value to the slightly smaller minimum value  $3.189 \text{ \AA}$ , which is slightly

larger than the value  $\delta z_0 = 3.176 \text{ \AA}$  for the free wavepacket.

The following subsections summarize the results for the chosen initial wavefunction which serves as a reference. Subsequent subsections consider extended results for electronic excited states of the target ion, or different kinetic energies of the free electron. Finally, we shall also consider the complementary scenario of indistinguishable electrons.

### 4.1 Dominant forward scattering versus negligible ionization or electron exchange processes

For the present example, the dominant effects of  $e + H_2^+$  scattering are obvious from the snapshot of the density of the wavefunction at  $t = 227 \text{ as}$ , which is shown in Figure 4. It penetrates almost exclusively into the domain B for forward scattering of electron “1”. On the logarithmic scale of Figure 4, one also notices marginal signatures of the “tails” of the wavefunction which leak out from domain B into E and H, corresponding to forward scattering of electron “1” and simultaneous ionization of electron 2, with about equal probabilities for the forward (E) and back (H) directions.

The corresponding time evolutions of the probabilities  $P_X(t)$  for populating domains  $X = A, I, B, E, H$  are shown in Figure 5 — all other populations for processes which

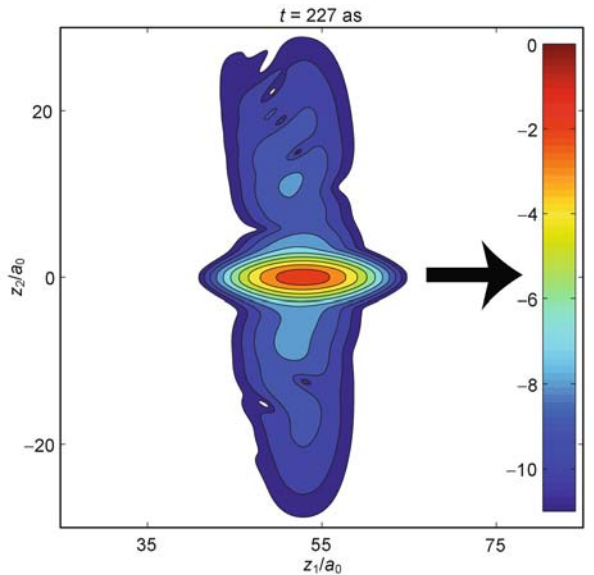


**Figure 4** Snapshot of the wavefunction  $\Psi_{l=0,k,\sigma}(z_1, z_2, t)$  representing  $e + H_2^+$  scattering, starting from  $H_2^+$  in the electronic ground state ( $l = 0$ ), with distinguishable, initially free and bound electrons “1” and “2”, respectively. The wavefunction is documented by colour-coded equidensity contours on the logarithmic scale. It has been propagated on the soft Coulomb potential adapted from ref. [62], as illustrated in Figure 2, starting at initial time  $t_{\text{in}} = -60 \text{ as}$ . The parameters  $k$  for the wavenumber of the incoming electron correspond to the asymptotic collision energy  $E_{\text{kin,asym}} = 1.5 \text{ keV}$ , cf. eqs. (7)–(9). The width parameter  $\sigma$  corresponds to the target width  $\delta z_0 = 3.176 \text{ \AA}$  at the instant of collision,  $t = 0$ , eq. (10). The arrow indicates the dominant direction of propagation.

involve electron exchange are even much smaller than  $10^{-6}$ . Accordingly, the wavepacket dynamics discovers almost exclusive transition A $\rightarrow$ I $\rightarrow$ B, i.e. forward scattering of electron “1” via the interaction domain I, with collision (“col”) time corresponding to the transient population of interaction domain I,  $\tau_{\text{col}} \approx 50$  as; the quantitative value of  $\tau_{\text{col}}$  depends on the choice of the boundaries of domain I, cf. Figure 2(b); for comparison, the time it takes to run across the internuclear distance  $R$  may be estimated as  $(R + \delta z_0)/(\hbar k/m_e) = 15$  as. In any case, the observation of almost exclusive electron forward-scattering is non-trivial because in principle, the total energy of the wavepacket suffices in order to induce all other competing processes, including ionizations and exchange of electrons, with corresponding wavepackets that would enter the other domains C-H in Figure 2. Apparently, the ultrafast collision time of just 50 as imposes strong dynamical constraints on the collision process, i.e. it is too short for efficient interactions of the two electrons which could cause any competing effects, beyond forward scattering of electron “1”.

#### 4.2 Dominant elastic versus small amounts of inelastic forward scattering

Next we zoom into further details of the process A $\rightarrow$ I $\rightarrow$ B in order to investigate whether forward scattering of electron “1” is exclusively elastic, or whether there are any inelastic effects of electron-electron interaction. For this purpose, we ignore any marginal penetrations of the wavefunctions into complementary domains. Accordingly, the quantum dynamics simulations may be carried out on the restricted rectangular grid covering domains A, I, B, with corresponding grid boundaries  $-z_{r,2,\min} = z_{r,2,\max} = 13.2$  Å for motions of electron

“2” along  $z_2$ . The reduction from  $z_{2,\max} = 92.6$  Å to  $z_{r,2,\max} = 13.2$  Å allows us to afford a rather systematic investigation of the details of the forward scattering of electron “1” from domain A via I to B, using an even larger upper limit  $z_{r,1,\max} = 914.1$  Å of the rectangular grid.

The analysis of the details of the forward scattering  $e + H_2^+ \rightarrow H_2^+ + e$  of electron “1”, for the present example, starts with the evaluation of the  $n \leftarrow l = 0$  transition probabilities  $P_{n,l=0,k,\sigma}$ , using the wavefunction  $\Psi_{n=0,k,\sigma}(z_1, z_2, t)$  on the rectangular grid, as outlined in section 3. The results are listed in Table 1. In accord with the snapshot shown in Figure 4, the elastic transition  $n = 0 \leftarrow l = 0$  is entirely dominant. In addition, we discover a small but significant transition to the first excited state. By comparison, the transitions to higher states are entirely negligible.

#### 4.3 Interplay of correlated elastic and uncorrelated inelastic forward scattering, and collision induced entanglement

Next we analyze the mechanism that causes the small inelastic deviation from pure elastic forward scattering of electron “1”. For this purpose, we employ the suggested time-dependent extension of scattering theory for analysis of the effects of electron-electron interaction (cf. section 3). Accordingly, we evaluate the uncorrelated and correlated partial waves, as outlined in section 3. The expansion of the total wavefunction in terms of these partial waves reveals only three significant contributions: As one may anticipate, by far the most important component is the one for uncorrelated elastic forward scattering, i.e., electron “1” runs across the two protons without any significant interaction with the other

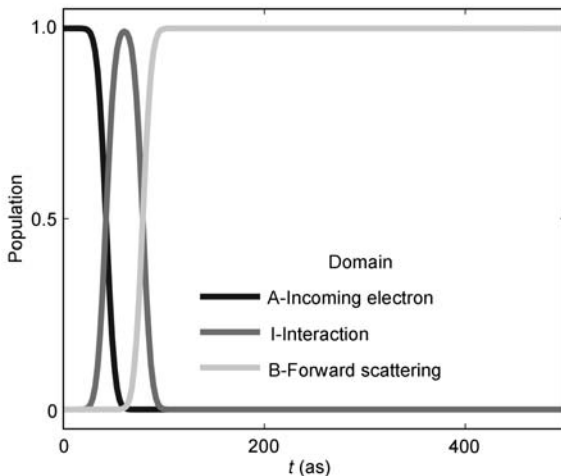


**Figure 5** Populations  $P_{X,l=0,k,\sigma}$  of domains  $X$  versus time, for the wavefunction  $\Psi_{l=0,k,\sigma}$  representing  $e + H_2^+$  scattering, eq. (29). The scenario of distinguishable electrons, and the parameters for the initial ground state  $l = 0$ , wavenumber  $k$  and width  $\sigma$  are the same as for the wavefunction shown in Figure 4. Domains A, I, B, C, E and H with the corresponding processes are specified in Figure 2. The population dynamics indicates dominant transition A $\rightarrow$ I $\rightarrow$ B from the reactants (A) via the strong interaction region (I) to forward scattering (B) of electron “1”, with two marginal subsequent processes B $\rightarrow$ E and B $\rightarrow$ H for ionization of electron “2” into the forward and backward directions, respectively. All other processes, which involve exchange of electrons “1” and “2”, are entirely negligible.

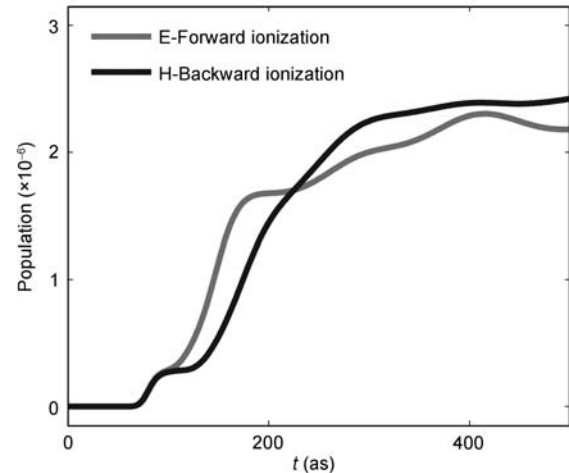


**Table 1** Elastic  $l \leftarrow l$  and inelastic  $n(\neq l) \leftarrow l$  electronic transition probabilities  $P_{n,l,k,\sigma}$  for the target ion  $\text{H}_2^+$  with electron “2”, induced by forward scattering of electron “1”

$n$	0.5 keV	1.0 keV	1.5 keV		
	$n \leftarrow 0$	$n \leftarrow 0$	$n \leftarrow 0$	$n \leftarrow 1$	$n \leftarrow 2$
0	0.9959	0.9987	0.9993	$6.52 \times 10^{-4}$	$1.32 \times 10^{-5}$
1	$3.91 \times 10^{-3}$	$1.29 \times 10^{-3}$	$6.60 \times 10^{-4}$	0.9980	$1.12 \times 10^{-3}$
2	$1.23 \times 10^{-4}$	$2.99 \times 10^{-5}$	$1.51 \times 10^{-5}$	$1.14 \times 10^{-3}$	0.9978
3	$8.81 \times 10^{-6}$	$2.09 \times 10^{-6}$	$9.64 \times 10^{-7}$	$1.29 \times 10^{-3}$	$9.42 \times 10^{-4}$

The results are derived from representative wavefunctions  $\Psi_{l,k,\sigma}(z_1, z_2, t)$  with quantum numbers  $l = 0, 1$ , or  $2$  for the initial electronic state (cf. Figure 3 and eqs. (30)–(33)). The width parameter  $\sigma$  is the same as the one which has been used for the results shown in Figures (4)–(9). The wave numbers  $k$  correspond to asymptotic kinetic energies  $E_{\text{kin,asym}} = 1.5$  keV (the same as in Figures (4)–(9)), 1.0 and 0.5 keV.

electron “2”. We note in passing that this uncorrelated elastic partial wave exhibits just marginal dispersion, in accord with eqs. (10), (14) for the rather slow dispersion of the free wavepacket — this supports our choice of the free wavepacket as a reference, for construction of the initial wavefunction (6), (10). The other two significant albeit small contributions are for correlated elastic forward scattering  $n = 0 \leftarrow l = 0$  and for uncorrelated inelastic  $1 \leftarrow 0$  scattering, see the components for  $c_{n=0,l=0,k,\sigma}^{(\text{cor})}(t)\Psi_{n=0,k,\sigma}^{\text{cor}}(z_1, z_2, t)$  and  $c_{n=1,l=0,k,\sigma}^{(\text{unc})}(t)\Psi_{n=1,k,\sigma}^{\text{unc}}(z_1, z_2, t)$  in eq. (34), respectively — all others are negligible. If one subtracts the dominant contribution for uncorrelated elastic forward scattering from the total wavefunction, the complementary partial wave, written as

$$\Delta\Psi_{l=0,k,\sigma}(z_1, z_2, t) = \Psi_{l=0,k,\sigma}(z_1, z_2, t) - c_{n=0,l=0,k,\sigma}^{(\text{unc})}(t)\Psi_{n=0,k,\sigma}^{\text{unc}}(z_1, z_2, t), \quad (43)$$

consists, therefore, of essentially just these two important partial waves, cf. eq. (34). The corresponding time dependent densities are illustrated by three subsequent snapshots in the top row of Figure 6. Apparently, it consists of two “head” and “tail” components which run slightly more rapidly and slightly slower than the dominant, uncorrelated elastic reference,  $\Psi_{n=0,k,\sigma}^{\text{unc}}(z_1, z_2, t)$ , respectively. As a consequence, these small head and tail components of  $\Delta\Psi_{l=0,k,\sigma}(z_1, z_2, t)$  contribute to the small dispersion of  $\Psi_{l=0,k,\sigma}(z_1, z_2, t)$ . Moreover, the centers of the head and tail parts oscillate along  $z_2$ , with opposite phases, indicating coherent oscillations of electron “2” in a hybrid state which consists of dominantly the ground state plus a small contribution of the first excited state. These oscillations are documented by means of two trajectories for the centers (i.e. the mean values of coordinates  $z_1$  and  $z_2$ ) of the head and tail parts, which are shown versus  $t$  and versus  $z_2$ , in the middle and bottom rows of Figure 6, respectively. Accordingly, the period of the oscillation,  $\tau_{01} \approx 340$  as corresponds to the energy gap  $E_1 - E_0$  between the electronic ground and first excited state which contribute to the hybrid state,

$$\tau_{01} \approx \frac{\hbar}{E_1 - E_0} = 329 \text{ as.} \quad (44)$$

In order to discover the origin of the oscillations of the head and tail parts of  $\Delta\Psi_{l=0,k,\sigma}(z_1, z_2, t)$ , we show a snapshot of its flux density, in Figure 7(a). For reference, illuminating

analyses of the mechanisms of electron dynamics in terms of flux densities has been demonstrated recently in refs. [87,88]. Here the snapshot is taken at time  $t = 0$ , i.e. at the instant of the collision, with large overlap of the wavefunction with the domains of the nuclei. Apparently, the two potential minima of the soft Coulomb potential at the two nuclei (cf. Figure 2) attract small parts of the incoming wavefunction, causing small momentum transfer from electron “1” to “2” such that two small parts of the wavefunction representing electron “2” start to move along the same physical direction as electron “1”, i.e. towards the positive  $z_2$  direction. Accordingly, one component moves from the domain close to the proton at  $Z_1 = -R/2$  towards the center of the  $\text{H}_2^+$  ion, reducing the distance from the center. The other component moves from the domain close to the proton at  $Z_2 = +R/2$  towards even larger distances from the center. The effect may be interpreted as two “kicks” of electron “1” on electron “2”, mediated by the two nuclei. These “kicks” are not strong enough, however, to induce ionization. Instead they induce two oscillatory motions of electron “2”. The resulting amplitudes of these oscillations are slightly larger for the “kick” at the nucleus located at  $R/2$  than at  $-R/2$ , yielding the tail and the head lobes, respectively. The corresponding momentum transfers imply that electron “1” loses a tiny bit of momentum along  $z_1$  in the tail lobe, whereas it wins momentum in the head lobe, causing that slightly faster velocity of the head lobe as compared to the tail one, which has been documented in Figure 6. A cartoon of the mechanism is illustrated by two schematic trajectories for the centers of the head and tail parts of  $\Delta\Psi_{l=0,k,\sigma}(z_1, z_2, t)$  in Figure 7(b). The fact that the complementary partial wave (43) is not equal to zero implies that the wavefunction  $\Psi_{l=0,k,\sigma}(z_1, z_2, t)$  cannot be written as a simple product of wave functions for electrons “1” and “2” — this is in marked contrast from the chosen separable form of the initial product wavefunction (7). We conclude that during the ultrafast collision, electron-electron interaction induces entanglement between the two electrons. Nevertheless, since the partial product wavefunction for elastic uncorrelated forward scattering is dominant in eq. (34), the degree of entanglement is rather small.

#### 4.4 Electron plus $\text{H}_2^+$ scattering in electronic ground versus excited states

Next we investigate effects of e +  $\text{H}_2^+$  scattering, starting from

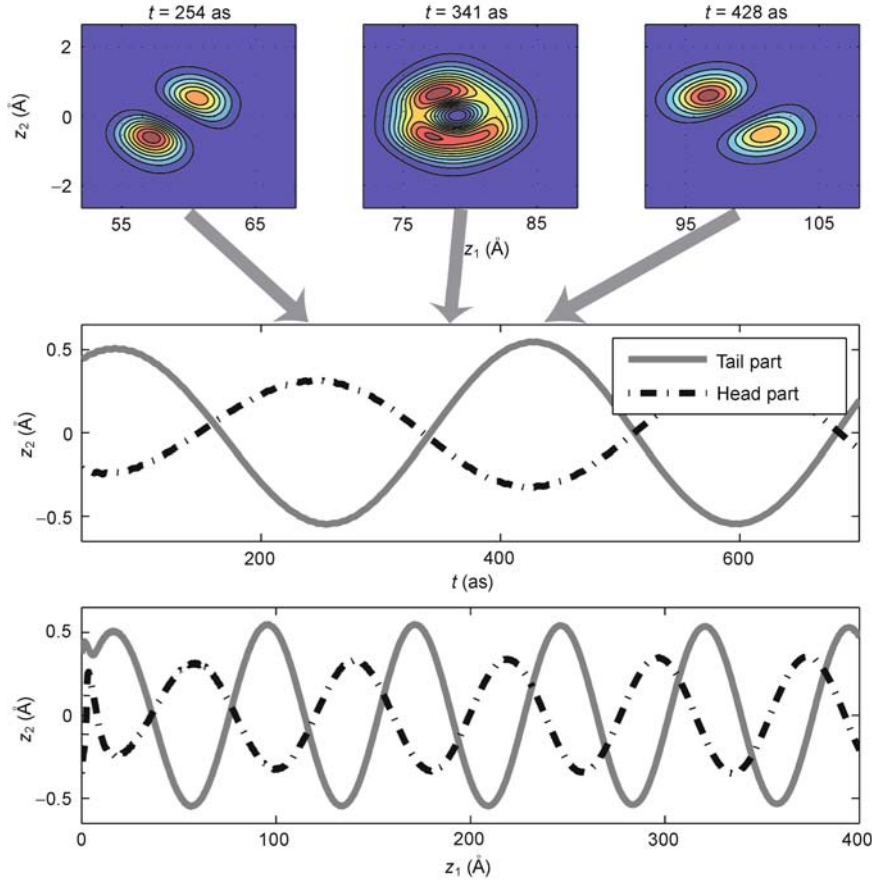


**Figure 6** Top panels: snapshots of the wavefunction  $\Delta\Psi_{l=0,k,\sigma}(z_1, z_2, t)$  which is defined in eq. (43), i.e. the wavefunction  $\Psi_{l=0,k,\sigma}(z_1, z_2, t)$  representing e +  $\text{H}_2^+$  scattering minus the partial wave for elastic uncorrelated forward scattering. The initial electronic state of model  $\text{H}_2^+$  is  $l = 0$ , and the parameters  $k$  and  $\sigma$  are the same as those used in Figures 4 and 5. The wavefunction may be considered as the sum of two parts which are separated by a line parallel to  $z_2$ , at  $z_1 = z_{1,\text{m}}(t)$ , where  $z_{1,\text{m}}(t)$  is the mean (“m”) value of  $z_1$ . These parts are referred to as “head” (“he”) and “tail” (“ta”), respectively. Middle and bottom panels:  $(z_2, t)$  and  $(z_1, z_2)$  representations of the trajectories of the mean values  $(z_{1,\text{he}}(t), z_{2,\text{he}}(t))$  and  $(z_{1,\text{ta}}(t), z_{2,\text{ta}}(t))$  of the head and tail parts of  $\Delta\Psi_{l=0,k,\sigma}(z_1, z_2, t)$ , respectively.

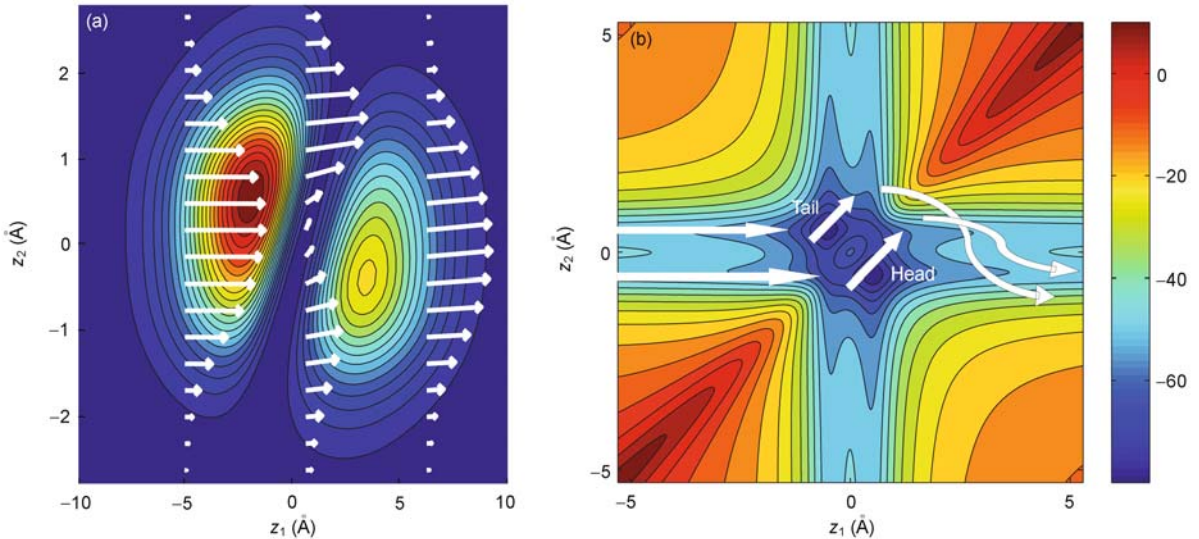


**Figure 7** Densities and flux densities of wavefunction  $\Delta\Psi_{l=0,k,\sigma}(z_1, z_2, t)$  at the instant of collision ( $t = 0$ ), illustrated by equidensities and by arrows, respectively, as defined and specified in eq. (43) and for Figure 6, respectively. Comparison of the two potential minima of the soft Coulomb potential (Figure 2) indicates momentum transfer from electron “1” to “2” mediated by the two protons, see the text. The parameters  $k$  and  $\sigma$  are the same as those used in Figures 4–6.

$H_2^+$  in excited electronic states,  $l = 1, 2$ , cf. Figure 3, again for the scenario of distinguishable electrons. For this purpose, we propagate and analyze the wavefunctions  $\Psi_{l,k,\sigma}(z_1, z_2, t)$ , using the same techniques which have been employed previously for  $l = 0$ . In order to compare the results and in accord with the experimental setup (section 2), we use the same parameters  $k$  and  $\sigma$ , corresponding to asymptotic kinetic energy  $E_{\text{kin,asym}} = 1.5$  keV and the target width  $\delta z_0 = 3.176 \text{ \AA}$ , respectively. It turns out that again, forward scattering of electron “1” is the dominant process.

The transition probabilities  $P_{n,l,k,\sigma}$  for  $l = 1, 2$  are compared with those for  $l = 0$  in Table 1. Apparently, elastic  $l \leftarrow l$  forward scattering is always dominant, but the amount of inelastic scattering increase systematically with  $l$ , i.e. if  $H_2^+$  is pre-excited from  $l = 0$  to  $l = 1$  or even more to  $l = 2$ , then it is “easier” to induce electronic transitions by means of electron scattering, including excitations and also de-exitations. Note that the corresponding scattering matrix is symmetric if the processes are carried out with the same total energy. The fact that the  $3 \times 3$  submatrix of the transition probabilities is not perfectly symmetric is due to the fact that we employ the same asymptotic kinetic energies; adding increasing energies of electronic excitations  $E_0, E_1, E_2$  yields systematic (albeit relatively small) increases of the total energies, thus breaking the ideal symmetry of the scattering matrix at constant total energy.

Most important for measuring molecular electron densities and their attosecond dynamics with diffraction is to have an influence of the electronic distributions of the target on the scattering phase. Such influence was approximated classically for molecular crystals in ref. [8] and should give rise to changes in Bragg spots intensities when the electronic structure in the molecule is changing. From a quantum mechanical perspective, we need to consider four contributions to the scattering phase: First, a given electron density (eigenstate) results in an elastic uncorrelated phase shift of the scattering electron as a result of its elastic (soft) Coulomb interactions with the nuclei but irrespective of the electron(s) of the target; second, an elastic correlated contribution due to interaction of the scattering and bound electrons; third an inelastic contributions (not considered in ref. [8]) can also result in changes of the transmitted energy and phase; and fourth, quantum entanglement needs to be considered because it can link the phase shifts between the oscillating bound electron and the scattered one. Our findings with respect to the elastic correlated and inelastic contributions show a clear effect of the molecule’s electron density distribution; this supports the possibility of using diffraction for imaging molecular states and their dynamics. Of even more interest for us, however, is a novel finding that is related to entanglement on attosecond time scales; this is discussed in the following.

#### 4.5 Effects of entangled free and bound electrons on time-dependent phases

The increased complexity of the  $P_{n,l>0,k,\sigma}$  compared to

$P_{n,l=0,k,\sigma}$  is associated with more complex mechanisms that show up in the corresponding wavefunctions  $\Delta\Phi_{l>0,k,\sigma}$  (not shown) as compared to  $\Delta\Phi_{l=0,k,\sigma}$ , cf. eq. (43) and Figures 6 and 7. In any case, our time-dependent extension of scattering theory suggests that the different dynamics of the wavefunctions for electron scattering off  $H_2^+$  in the electronic ground ( $l = 0$ ) versus excited ( $l > 0$ ) states should also show up in corresponding differences of the time-dependent phase shifts  $\eta_{l=0,k,\sigma}(t)$  versus  $\eta_{l>0,k,\sigma}(t)$ . Note that the time-dependent phase shifts we discuss here are different from the constant phase shifts that result from traditional electron beam experiments; asymptotically, they approach the values which are detected by means of Bragg diffraction [8]. Since our propagation of the representative wavepackets on large, albeit finite grids does not allow any asymptotic determinations of the absolute phase shifts, we choose a pragmatic time dependent approach. For any time  $t$ , we determine the peaks ( $p(t)$ ) of the wavefunctions  $\max|\Psi_{l,k,\sigma}(z_1, z_2, t)|$  at  $(z_1, z_2) = (z_{1,p(t)}, z_{2,p(t)})$  together with the corresponding amplitudes and relative phases

$$\begin{aligned} \Psi_{l,k,\sigma}(z_1, z_{2,p(t)}, t) = \\ |\Psi_{l,k,\sigma}(z_1, z_{2,p(t)}, t)| \exp(i\delta\eta_{l,k,\sigma}(z_1, z_{2,p(t)}, t)), \end{aligned} \quad (45)$$

where

$$\delta\eta_{l,k,\sigma}(z_1, z_{2,p(t)}, t) = \eta_{l,k,\sigma}(z_1, z_{2,p(t)}, t) - \eta_{l,k,\sigma}(z_{1,p(t)}, z_{2,p(t)}, t). \quad (46)$$

Note that by definition,

$$\delta\eta_{l,k,\sigma}(z_1 = z_{1,p(t)}, z_{2,p(t)}, t) = 0 \quad (47)$$

at the peak of the wavefunctions.

Because the wavefunctions are dominated by the contribution for elastic uncorrelated forward scattering of electron “1”, the relative phases are dominated by the “kinetic” contribution of momentum to the relative phase shifts due to (soft) Coulomb scattering, analogous and close to the expression  $ik(z_1 - z_{1,p(t)})$  for the free wave packet [79]. Since we use the same wavenumbers corresponding to the same asymptotic kinetic energies  $E_{\text{kin,asym}}$ , these “kinetic” contributions for uncorrelated elastic electron scattering (that means without electron-electron interaction) should be the same for all wavefunctions  $\Psi_{l,k,\sigma}(z_1, z_2, p, t)$  representing  $e + H_2^+$  scattering, irrespective of the initial electronic state  $l$ . In addition, there are “dynamical” contributions due to the different processes of correlated elastic as well as inelastic scattering (that means with electron-electron interaction) that depend on  $l$ , as discovered for the different inelastic transition probabilities depending on  $l$ , cf. Table 1. Hence, if one subtracts two relative phases from each other, say

$$\begin{aligned} \Delta\eta_{n,l,k,\sigma}(z_1, z_{2,p(t)}, t) = \delta\eta_{n,k,\sigma}(z_1, z_{2,p(t)}, t) \\ - \delta\eta_{l=0,k,\sigma}(z_1, z_{2,p(t)}, t), \end{aligned} \quad (48)$$

then the dominant “kinetic” contributions should cancel so that the “dynamical” ones become more obvious. Exemplarily, we consider the difference of the relative phases

(48) for electron scattering off  $H_2^+$  in the electronic ground ( $l = 0$ ) and first excited ( $n = 1$ ) states. It turns out that  $\Delta\eta_{n=1,l=0,k,\sigma}(z_1, z_2, p(t), t)$  is close to zero, i.e. at the collision energy  $E_{kin,max} = 1.5$  keV, kinetic effects of momentum on the relative phases are much larger than dynamical ones. Nevertheless, we shall now show that the small dynamical effects are significant. Specifically, it turns out that in accord with eq. (47),  $\Delta\eta_{n=1,l=0,k,\sigma}(z_1, z_2, p(t), t)$  varies approximately linearly with the distance  $z_1$  from the peak of the wavefunction at  $z_{1,p(t)}$ ,

$$\begin{aligned} & \Delta\eta_{n=1,l=0,k,\sigma}(z_1, z_2, p(t), t) \\ & \approx \Delta\eta'_{n=1,l=0,k,\sigma}(z_1, z_2, p(t), t)(z_1 - z_{1,p(t)}), \end{aligned} \quad (49)$$

where  $\Delta\eta'$  denotes the  $\frac{\partial}{\partial z_1}$  derivative or the “slope” of  $\Delta\eta$ . The time evolution of this “slope” of the difference of the relative phases of the wavefunctions for  $e + H_2^+$  scattering with  $H_2^+$  in electronic states  $n = 1$  and  $l = 0$  is documented in Figure 8. Apparently, the “slope” exhibits quasi-periodic oscillations, with peaks of the order of  $0.2/\text{\AA}$  above the zero base line, and with period of ca 150 as, which is about half the periods  $\tau_{01}$  or  $\tau_{12}$  which are associated with the energy gaps for the dominant transitions to neighbouring levels of  $H_2^+$  in levels  $l = 0$  or  $n = 1$ , eq. (44), see also the oscillations of the “head” and “tail” components of the wavefunction documented in Figure 6. We conclude that the related effects of inelastic as well as elastic uncorrelated  $e + H_2^+$  forward scattering determine the time evolution of the slope of the difference of the relative phases,  $\Delta\eta'_{n=1,l=0,k,\sigma}(z_1, z_2, p(t), t)$  or, in other words,  $\Delta\eta'_{n=1,l=0,k,\sigma}(z_1, z_2, p(t), t)$  carries information about the dynamics of  $e + H_2^+$  scattering. Note that  $\Delta\eta'$  is a quantity which depends on the coordinate  $z_1$  of the scattered electron “1”. The fact that  $\Delta\eta'$  exhibits quasi-periodic oscillations which reflect the collision induced dynamics of electron “2” in the target,  $H_2^+$ , may be considered as signature of small but significant entanglement of the free and bound electrons, after collision.

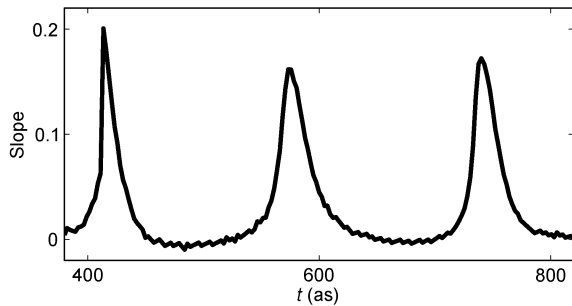


**Figure 8** The “slope”, i.e. the  $z_1$ -derivative of the difference of the relative phases  $\delta\eta_{1,k,\sigma}(z_1, z_2 = 0, t)$  minus  $\delta\eta_{0,k,\sigma}(z_1, z_2 = 0, t)$ , for the wavefunctions representing  $e + H_2^+$  scattering, with  $H_2^+$  in the first excited electronic and in the ground state, respectively, eq. (48). The parameters  $k$  and  $\sigma$  are the same as those used in Figures 4–7.

#### 4.6 Effects of increased kinetic energies on $e + H_2^+$ scattering

In order to extrapolate the present results for the model  $e + H_2^+$  scattering from collision energy  $E_{kin,asym} = 1.5$  keV to typical experimental values of 30 keV (see section 2), we have also carried out quantum model simulations for the same scenario, e.g. again with  $H_2^+$  in the electronic ground state  $l = 0$ , but with lower asymptotic kinetic energies,  $E_{kin,asym} = 0.5$  and 1.0 keV. The resulting elastic and inelastic transition probabilities for electron forward scattering are also documented in Table 1. These results reveal a systematic trend, i.e. the dominance of elastic electron forward scattering increases with collision energy, at the expense of inelastic transitions. This can be rationalized by the fact that the collision time  $\tau_{col}$ , i.e. the time when electron “1” passes through the domain “I” of strong interactions with electron “2” (see Figure 2(b)), decreases with increasing kinetic energies. This means that the time for efficient inelastic or elastic correlated effects decreases, rendering those processes more and more inefficient. By extrapolation, the collision time  $\tau_{col} = 11.2$  as for the experimental  $E_{kin,asym} = 30$  keV is smaller than  $\tau_{col} = 50$  as for  $E_{kin,asym} = 1.5$  keV, by a factor 4.5. We may, therefore, anticipate that inelastic and correlated elastic processes are reduced similarly at  $E_{kin,asym} = 30$  keV, compared to the present model results at  $E_{kin,asym} = 1.5$  keV. More quantitative results about the amount of reduction would require quantum model simulations analogous to the present ones, but with ca 20 times larger kinetic energies, or about  $\sqrt{20}$  times larger momenta, or with about  $1/\sqrt{20}$  times smaller spatial grid spacings, or with about 20 times larger 2D-grids — this is possible, in principle, but beyond our present computational resources, see the discussion at the beginning of this section.

#### 4.7 Equivalent results for $e + H_2^+$ scattering with indistinguishable versus distinguishable electrons

Finally, let us consider briefly the second scenario of  $e + H_2^+$  scattering, with indistinguishable electrons in a singlet or triplet states. As discussed in section 3, the corresponding spatial wavefunction  $\Psi_{l,k,\sigma,\pm}(z_1, z_2, t)$  may be generated from the wavefunction  $\Psi_{l,k,\sigma}(z_1, z_2, t)$  for distinguishable electrons, simply by symmetrization or antisymmetrization, respectively, cf. eq. (41). Exemplarily, Figure 9 shows a snapshot of the density of  $\Psi_{l=0,k,\sigma,\pm}(z_1, z_2, t)$  for  $e + H_2^+$  model scattering with indistinguishable electrons, for the same initial conditions and parameters  $l = 0, k, \sigma$  and also for the same time  $t = 227$  as, as those used in Figure 4 for indistinguishable electrons. Apparently, the densities are essentially the same for the free and bound electrons in singlet or triplet states, i.e. the spin does not matter. Moreover, the symmetrized or antisymmetrized wavefunction consist of two equivalent partial waves which can be interpreted as representations of two collision processes of distinguishable electrons, one for scattering of the free electron “1” with electron “2” bound in  $H_2^+$ ,

and vice versa for the other process. The partial waves for the two processes overlap when they run through the domain “I” for strong interactions (cf. Figure 2), but asymptotically, there are no significant interferences whatsoever. As a consequence, all the analyses which have been carried out above for the first scenario of indistinguishable electrons are also applicable for the second one with distinguishable electrons, at least in the asymptotic domain. The reason is that for the present kinetic energy  $E_{\text{kin,asym}}$ , which is much larger than the ionization potential IP of the target ion, forward scattering of the electrons into domains B and C (cf. Figure 2) is much faster than subsequent ionizations, which are documented by (logarithmically!) small amounts of the wavefunctions which leak out from domain B into E and H, and likewise from D into E and F. By extrapolation, one may employ the representative first scenario also for the experimental situation with 30 keV electron scattering. Only at much smaller collision energies approaching the ionization potential, one may anticipate that electron forward scattering and collision induced ionization may proceed with similar velocities — this would cause interferences of the partial waves representing ionization of one or the other of the indistinguishable electrons, different from the results for the scenario of distinguishable electrons.

## 5 Conclusions

The reported results have several important implications for

experiments aiming to visualize electron dynamics in four dimensions and on attosecond time scales. The extremely short duration and strong spatial localization of attosecond electron packets does not significantly increase the radiation damage; ionization and/or exchange of electrons only occurs with probabilities below  $10^{-6}$ . The here reported trend, that higher electron energies lead to shorter collision times and to less inelastic contributions, is related to the experimental observation in condensed matter of a decreasing stopping power for increasing collision energies above  $\sim 1$  keV [89,90]. It would be interesting, in supplementary studies, to also investigate the influence of the packet duration and the role of the lower ionization potentials of more complicated molecules, but the results reported here are already supportive for experiments.

The scattering process transfers some momentum to the bound electron and induces small-amplitude motions of the charge density with quasi-periodic attosecond recurrences. The mechanism is independent of energetic resonances and is effective for arbitrary molecular systems without limitation by selection rules for transitions between eigenstates. This provides the possibility to excite some types of ultrafast electron dynamics that is not easily accessible by photon-based pump sources. In combination with a second, delayed attosecond electron packet, a pump-probe experiment is conceivable that works entirely with electron pulses.

Our studies reveal several mechanisms of how changes of molecular charge density can affect the phase of the outgoing electron wave. This influence is required in order to have the intensity of diffraction features, such as Bragg spots, depend on dynamical changes of charge density in the molecular system or crystal. Snapshots with attosecond timing can provide the dynamics of a changing electron density, for example in a pump-probe-type experiment. Some of the predicted phase shifts are result of inelastic interactions and entanglement. The creation of an oscillating wavepacket in the target is result of an entangling scattering process and the outgoing electron phase is therefore also oscillating in time with similar attosecond periodicities. This new effect, which is the result of attosecond momentum transfers, might be measurable as an intensity modulation in an electron beam interferometer with variable path lengths, maybe in an arrangement that is used for detecting other types of phase shifts [91]. For attosecond diffraction, the uncorrelated elastic forward scattering is the dominant contribution to the measured time-dependent phase shift, which contains information about the electron density of the target. Other types of scattering phase shifts are small but significant. Correlated elastic, and inelastic scattering contains information about dynamical and entangling effects, calling for considerations in the experimental conception. Concerning the theory and techniques for quantum dynamics simulations of electron pulse scattering off molecules and ions, we have suggested and applied a time-dependent extension of the traditional time-independent scattering theory, in order to account for the impulsive na-

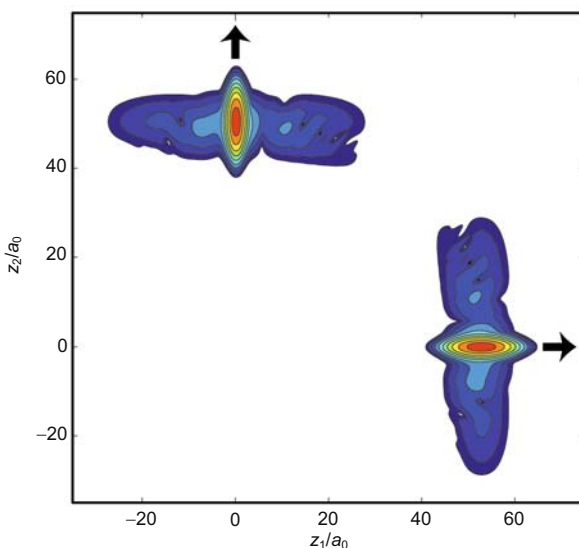


**Figure 9** Snapshot of the same densities of the wavefunction  $\Psi_{l=0,k,\sigma,+}(z_1, z_2, t)$  and  $\Psi_{l=0,k,\sigma,-}(z_1, z_2, t)$  representing  $e + H_2^+$  scattering for the second scenario of indistinguishable electrons in the singlet and triplet states, i.e. with antisymmetric and symmetric nuclear spin functions, respectively. The quantum numbers, parameters and notations are the same as those used in Figures 4–8. The spatial wavefunctions have been generated by symmetrization or antisymmetrization of the wavefunction shown in Figure 4, cf. eq. (41).

ture of momentum transfer mediated by the nuclei, during the ultrafast collision, with collision times in the sub-100 fs domain. Moreover, we could show that for collision energies in the keV domain, two scenarios of indistinguishable and distinguishable free and bound electrons yield equivalent results, irrespective of the electronic spins. As a consequence, we recommend to employ the scenario of distinguishable free and bound electrons for future calculations, allowing an enormous reduction of the computational resources.

Taken as a whole, the results here demonstrate the high value of quantum model simulations, even simple ones, for discovery and for understanding the mechanisms of scattering and diffraction on attosecond time scales; the reported and forthcoming results will prove essential for the experimental realization of attosecond four-dimensional imaging.

We are grateful to Prof. Bandrauk A. D. and to Dr. Smirnova O. for valuable hints to the literature and to Dr. Schmidt B. for support with the WavePacket program. Generous financial support by the Rudolf-Kaiser-Stiftung and the Munich Centre for Advanced Photonics as well as by Deutsche Forschungsgemeinschaft (Grant No. Sfb 450 TP C1) and Fonds der chemischen Industrie to P.B. and J.M., respectively, is also gratefully acknowledged.

- 1 Zewail A H. In: Frängsmyr T, ed. Les Prix Nobel: The Nobel Prizes 1999. Stockholm: Almqvist & Wiksell, 2000. 110
- 2 Baum P, Yang D S, Zewail A H. 4D visualization of transitional structures in phase transformations by electron diffraction. *Science*, 2007, 318: 788–792
- 3 Remacle F, Levine R D. An electronic time scale in chemistry. *Proc Natl Acad Sci USA*, 2006, 103: 6793–6798
- 4 Kuleff A I, Cederbaum L S. Tracing ultrafast interatomic electronic decay processes in real time and space. *Phys Rev Lett*, 2007, 98: 083201
- 5 Geppert D, von den Hoff P, de Vivie-Riedle R. Electron dynamics in molecules: A new combination of nuclear quantum dynamics and electronic structure theory. *J Phys B*, 2008, 41: 074006
- 6 Bandrauk A D, Chelkowski S, Corkum P B, et al. Attosecond photoionization of a coherent superposition of bound and dissociative molecular states: Effect of nuclear motion. *J Phys B*, 2009, 42: 134001
- 7 Bandrauk A D, Manz J, Vrakking M. Attosecond molecular dynamics, preface. *Chem Phys*, 2009, 366: 1
- 8 Baum P, Zewail A H. 4D attosecond imaging with free electrons: Diffraction methods and potential applications. *Chem Phys*, 2009, 366: 2–8
- 9 Farrell J P, McFarland B K, Gühr M, et al. Relation of high harmonic spectra to electronic structure in N<sub>2</sub>. *Chem Phys*, 2009, 366: 15–21
- 10 Lock R M, Zhou X, Lia W, et al. Measuring the intensity and phase of high-order harmonic emission from aligned molecules. *Chem Phys*, 2009, 366: 22–32
- 11 Trallero-Herrero C, Schmidt B E, Shiner A D, et al. High harmonic generation in ethylene with infrared pulses. *Chem Phys*, 2009, 366: 33–36
- 12 Sukiasyan S, McDonald C, Van Vlack C, et al. Correlated few-electron dynamics in intense laser fields. *Chem Phys*, 2009, 366: 37–45
- 13 Kato T, Kono H. Time-dependent multiconfiguration theory for ultrafast electronic dynamics of molecules in an intense laser field: Electron correlation and energy redistribution among natural orbitals. *Chem Phys*, 2009, 366: 46–53
- 14 Chirilă C C, Lein M. High-order harmonic generation in vibrating two-

- electron molecules. *Chem Phys*, 2009, 366: 54–57
- 15 Morales F, Pérez-Torres J F, Sanz-Vicario J L, et al. Probing H<sub>2</sub> quantum autoionization dynamics with XUV atto and femtosecond laser pulses. *Chem Phys*, 2009, 366: 58–63
- 16 Nguyen-Dang T T, Peters M, Wang S M, et al. Toward *ab initio* simulations of multiple ionization processes in intense laser field. *Chem Phys*, 2009, 366: 71–84
- 17 Milošević D B, Busuladžić M, Gazibegović-Busuladžić A, et al. Strong-field approximation for high-order above-threshold ionization of randomly oriented diatomic molecules. *Chem Phys*, 2009, 366: 85–90
- 18 Son S K, Chu S I. Theoretical study of orientation-dependent multiphoton ionization of polyatomic molecules in intense ultrashort laser fields: A new time-dependent Voronoi-cell finite difference method. *Chem Phys*, 2009, 366: 91–102
- 19 Yonehara T, Takatsuka K. Characterization of electron-deficient chemical bonding of diborane with attosecond electron wavepacket dynamics and laser response. *Chem Phys*, 2009, 366: 115–128
- 20 Periyasamy G, Levine R D, Remacle F. Electronic wave packet motion in water dimer cation: A many electron description. *Chem Phys*, 2009, 366: 129–138
- 21 von den Hoff P, Znakovskaya I, Kling M F, et al. Attosecond control of the dissociative ionization via electron localization: A comparison between D<sub>2</sub> and CO. *Chem Phys*, 2009, 366: 139–147
- 22 Zewail A H. 4D ultrafast electron diffraction, crystallography, and microscopy. *Annu Rev Phys Chem*, 2006, 57: 65–103
- 23 Gedik N, Yang D S, Logvenov G, et al. Nonequilibrium phase transitions in cuprates observed by ultrafast electron crystallography. *Science* 2007, 316: 425–429
- 24 Carbone F, Baum P, Rudolf P, et al. Structural preablation dynamics of graphite observed by ultrafast electron crystallography. *Phys Rev Lett*, 2008, 100: 035501
- 25 Yang D S, Lao C, Zewail A H. 4D electron diffraction reveals correlated unidirectional behavior in zinc oxide nanowires. *Science* 2008, 321: 1660–1664
- 26 Ruan C Y, Murooka Y, Raman R K, et al. Dynamics of size-selected gold nanoparticles studied by ultrafast electron nanocrystallography. *Nano Lett*, 2007, 7: 1290–1296
- 27 Chen S, Seidel M T, Zewail A H. Atomic-scale dynamical structures of fatty acid bilayers observed by ultrafast electron crystallography. *Proc Natl Acad Sci USA*, 2005, 102: 8854–8859
- 28 Gahlmann A, Park S T, Zewail A H. Structure of isolated biomolecules by electron diffraction-laser desorption: Uracil and guanine. *J Am Chem Soc*, 2009, 131: 2806–2809
- 29 Siwick B J, Dwyer J R, Jordan R E, et al. An atomic-level view of melting using femtosecond electron diffraction. *Science* 2003, 302: 1382–1385
- 30 Harb M, Ernstorfer R, Hebeisen C T, et al. Electronically driven structure changes of Si captured by femtosecond electron diffraction. *Phys Rev Lett*, 2008, 100: 155504
- 31 Wang X, Nie S H, Li J J, et al. Electronic Grüneisen parameter and thermal expansion in ferromagnetic transition metal. *Appl Phys Lett*, 2008, 92: 121918
- 32 Reckenthaler P, Centurion M, Fuß W, et al. Time-resolved electron diffraction from selectively aligned molecules. *Phys Rev Lett*, 2009, 102: 213001
- 33 Zewail A H, Thomas J M. 4D Electron Microscopy. London: Imperial College Press, 2009
- 34 Park H S, Kwon O H, Baskin J S, et al. Direct observation of martensitic phase-transformation dynamics in Iron by 4D single-pulse electron microscopy. *Nano Lett*, 2009, 9: 3954–3962

- 35 Barwick B, Park H S, Kwon O H, et al. 4D imaging of transient structures and morphologies in ultrafast electron microscopy. *Science*, 2008, 322: 1227–1231
- 36 Yurtsever A, Zewail A H. 4D nanoscale diffraction observed by convergent-beam ultrafast electron microscopy. *Science*, 2009, 326: 708–712
- 37 Carbone F, Kwon O H, Zewail A H. Dynamics of chemical bonding mapped by energy-resolved 4D electron microscopy. *Science*, 2009, 325: 181–184
- 38 Breidbach J, Cederbaum L S. Universal attosecond response to the removal of an electron. *Phys Rev Lett*, 2005, 94: 033901
- 39 Baum P, Zewail A H. Attosecond electron pulses for 4D diffraction and microscopy. *Proc Natl Acad Sci USA*, 2007, 104: 18409–18414
- 40 Hilbert S A, Uiterwaal C, Barwick B, et al. Temporal lenses for attosecond and femtosecond electron pulses. *Proc Natl Acad Sci USA*, 2009, 106: 10558–10563
- 41 Krausz F, Ivanov M. Attosecond physics. *Rev Mod Phys*, 2009, 81: 163–234
- 42 Corkum P B, Krausz F. Attosecond science. *Nature Phys*, 2007, 3: 381–387
- 43 Illenberger E, Momigny J. Gaseous Molecular Ions. An Introduction to Elementary Processes Induced by Ionization. New York: Springer, 1992
- 44 Gertitschke P L, Domcke W. Time-dependent wave-packet description of dissociative electron attachment. *Phys Rev A*, 1993, 47: 1031–1044
- 45 Lehr L, Manz J, Miller W H. A classical approach to resonant low energy electron scattering off molecules: Application to the  $a_1$ -shape resonance of  $\text{CF}_3\text{Cl}$ . *Chem Phys*, 1997, 214: 301–312
- 46 Harvey A G, Tennyson J. Electron re-scattering from  $\text{H}_2$  and  $\text{CO}_2$  using R-matrix techniques. *J Mod Opt*, 2007, 54: 1099–1106
- 47 Harvey A G, Tennyson J. Electron re-scattering from aligned linear molecules using the R-matrix method. *J Phys B-A Mol Opt Phys*, 2009, 42: 095101
- 48 Burke P G, Tennyson J. R-matrix theory of electron molecule scattering. *Mol Phys*, 2005, 103: 2537–2548
- 49 Gorfinkel J D, Faure A, Taioli S, et al. Electron-molecule collisions at low and intermediate energies using the R-matrix method. *Eur Phys J D*, 2005, 35: 231–237
- 50 Blanco F, Garcia G. Screening corrections for calculation of electron scattering differential cross sections from polyatomic molecules. *Phys Lett A*, 2004, 330: 230–237
- 51 Iga I, Lee M T, Bonham R A. Role of the intramolecular multiple scattering on electron diffraction from nitrogen molecule in the intermediate energy range. *J Mol Struc: Theochem*, 1999, 468: 241–251
- 52 Zuo T, Bandrauk A D, Corkum P B. Laser-induced electron diffraction: A new tool for probing ultrafast molecular dynamics. *Chem Phys Lett*, 1996, 259: 313–320
- 53 Spanner M, Smirnova O, Corkum P B, et al. Reading diffraction images in strong field ionization of diatomic molecules. *J Phys B*, 2004, 37: L243–L250
- 54 Yurchenko S N, Patchkovskii S, Litvinyuk I V, et al. Laser-induced interference, focusing, and diffraction of rescattering molecular photoelectrons. *Phys Rev Lett*, 2004, 93: 223003
- 55 Hu S X, Collins L A. Imaging molecular structures by electron diffraction using an intense few-cycle pulse. *Phys Rev Lett*, 2005, 94: 073004
- 56 Meckel M, Comtois D, Zeidler D, et al. Laser-induced electron tunneling and diffraction. *Science*, 2008, 320: 1478–1482
- 57 Morishita T, Okunishi M, Shimada K, et al. Retrieval of experimental differential electron-ion elastic scattering cross sections from high-energy ATI spectra of rare gas atoms by infrared lasers. *J Phys B: At Mol Opt Phys*, 2009, 42: 105205
- 58 Bandrauk A D, Chelkowski S, Diestler D J, et al. Quantum-mechanical models for photo-ionization: Uni-directional electron re-scattering by a laser pulse. *Int J Mass Spec*, 2008, 277: 189–196
- 59 Bandrauk A D, Manz J, Yuan K J. Electron wavepacket phases in ionization and rescattering processes by intense laser pulses. *Laser Phys*, 2009, 19: 1559–1573
- 60 Corkum P B. Plasma perspective on strong field multiphoton ionization. *Phys Rev Lett*, 1993, 71: 1994–1997
- 61 Bandrauk A D, Lu H. Laser-induced electron recollision in  $\text{H}_2$  and electron correlation. *Phys Rev A*, 2005, 72: 023408
- 62 Bandrauk A D, Chelkowski S, Kawai S, et al. Effect of nuclear motion on molecular high-order harmonics and on generation of attosecond pulses in intense laser pulses. *Phys Rev Lett*, 2008, 101: 153901
- 63 Walters Z B, Tonzanic S, Greene C H. Vibrational interference of Raman and high harmonic generation pathways. *Chem Phys*, 2009, 366: 103–114
- 64 Smirnova O, Mairesse Y, Patchkovskii S, et al. High harmonic interferometry of multi-electron dynamics in molecules. *Nature*, 2009, 460: 972–977
- 65 Morishita T, Le A T, Chen Z, et al. Accurate retrieval of structural information from laser-induced photoelectron and high-order harmonic spectra by few-cycle laser pulses. *Phys Rev Lett*, 2008, 100: 013903
- 66 Bandrauk A D, Chelkowski S, Diestler D J, et al. Quantum simulation of high-order harmonic spectra of the hydrogen atom. *Phys Rev A*, 2009, 79: 023403
- 67 Hu S X, Collins L A, Schneider B I. Attosecond photoelectron microscopy of  $\text{H}_2^+$ . *Phys Rev A*, 2009, 80: 023426
- 68 Yuan K J, Lu H, Bandrauk A D. LIED – Laser induced electron diffraction in  $\text{H}_2$  with linear and circular polarization ultrashort XUV laser pulses. *Phys Rev A*, 2009, 80: 061403
- 69 Dörner R, Bräuning H, Jagutzki O, et al. Double photoionization of spatially aligned  $\text{D}_2$ . *Phys Rev Lett*, 1998, 81: 5776–5779
- 70 Fernández J, Yip F L, Rescigno T N, et al. Two-center effects in one-photon single ionization of  $\text{H}_2^+$ ,  $\text{H}_2$ , and  $\text{Li}_2^+$  with circularly polarized light. *Phys Rev A*, 2009, 79: 043409
- 71 Barth I, Manz J, Paramonov G K. Time-dependent extension of Koopmans' picture for ionisation by a laser pulse: Application to  $\text{H}(B^1\Sigma_u^+)$ . *Mol Phys*, 2008, 106: 467–483
- 72 Taylor J R. Scattering Theory—The Quantum Theory of Nonrelativistic Collisions. New York: John Wiley & Sons, 1972
- 73 Glaeser R M. Review: Electron crystallography: Present excitement, a nod to the past, anticipating the future. *J Struct Biol*, 1999, 128: 3–14
- 74 Peng L M. Electron atomic scattering factors and scattering potentials of crystals. *Micron*, 1999, 30: 625–649
- 75 Stapelfeldt H, Seideman T. Colloquium: Aligning molecules with strong laser pulses. *Rev Mod Phys*, 2003, 75: 543–557
- 76 Filsinger F, Küpper J, Meijer G, et al. Quantum-state selection, alignment, and orientation of large molecules using static electric and laser fields. *J Chem Phys*, 2009, 131: 064309
- 77 Heller E J, Manz J. Dissociation of symmetry-adapted local modes studied by FFT-propagation of bond-adapted wavefunctions. *Z Phys D*, 1989, 13: 281–288
- 78 Peek J M. Eigenparameters of the 1s  $\sigma_g$  and 2p  $\sigma_u$  orbitals of  $\text{H}_2^+$ . *J Chem Phys*, 1965, 43: 3004
- 79 Tannor D J. Introduction to Quantum Mechanics—A Time Dependent Perspective. USA: University Science Books, 2007
- 80 Bisseling R H, Kosloff R, Manz J. Dynamics of hyperspherical and local mode resonance decay studied by time dependent wave packet propagation.

- tion. *J Chem Phys*, 1985, 83: 993–1004
- 81 Feit M D, Fleck Jr J A, Steiger A. Solution of the Schrödinger equation by a spectral method. *J Comp Phys*, 1982, 47: 412–433
- 82 Feit M D, Fleck Jr J A. Solution of the Schrödinger equation by a spectral method II: Vibrational energy levels of triatomic molecules. *J Chem Phys*, 1983, 78: 301–308
- 83 Leforestier C, Bisseling R, Cerjan C, et al. A comparison of different propagation schemes for the time dependent Schrödinger equation. *J Comput Phys*, 1991, 94: 59–80
- 84 Schmidt B, Lorenz U. WavePacket 4.6 (/4.7): A program package for quantum-mechanical wavepacket propagation and time-dependent spectroscopy. Available via <http://wavepacket.sourceforge.net> (2009)
- 85 Gonzalez-Lezana T, Rackham E J, Manolopoulos D E. Quantum reactive scattering with a transmission-free absorbing potential. *J Chem Phys*, 2004, 120: 2247–2254
- 86 Press W H, Teukolsky S A, Vetterling W T, et al. *Numerical Recipes in Fortran 90*. USA: Cambridge University Press, 1996
- 87 Okuyama M, Takatsuka K. Electron flux in molecules induced by nuclear motion. *Chem Phys Lett*, 2009, 476: 109–115
- 88 Barth I, Hege H C, Ikeda H, et al. Concerted quantum effects of electronic and nuclear fluxes in molecules. *Chem Phys Lett*, 2009, 481: 118–123
- 89 Inokuti M. Inelastic collisions of fast charged particles with atoms and molecules—The Bethe theory revisited. *Rev Mod Phys*, 1971, 43: 297–347
- 90 Jablonski A, Tanuma S, Powell C J. Modified predictive formula for the electron stopping power. *J Appl Phys*, 2008, 103: 063708
- 91 Caprez A, Barwick B, Batelaan H. Macroscopic test of the Aharonov-Bohm effect. *Phys Rev Lett*, 2007, 99: 210401